NASA/TM—2018–219863

Mechanisms of Oxide Formation in the Self-Reacting Friction Stir Weld Process

J.A. Schneider
The University of Alabama in Huntsville, Huntsville, Alabama

J.P. Norris and P. Chen
Jacobs ESSST, Marshall Space Flight Center, Huntsville, Alabama

A.C. Nunes, Jr.
Marshall Space Flight Center, Huntsville, Alabama

August 2018

The NASA STI Program…in Profile

Since its founding, NASA has been dedicated to the advancement of aeronautics and space science. The NASA Scientific and Technical Information (STI) Program Office plays a key part in helping NASA maintain this important role.

The NASA STI Program Office is operated by Langley Research Center, the lead center for NASA's scientific and technical information. The NASA STI Program Office provides access to the NASA STI Database, the largest collection of aeronautical and space science STI in the world. The Program Office is also NASA's institutional mechanism for disseminating the results of its research and development activities. These results are published by NASA in the NASA STI Report Series, which includes the following report types:

- TECHNICAL PUBLICATION. Reports of completed research or a major significant phase of research that present the results of NASA programs and include extensive data or theoretical analysis. Includes compilations of significant scientific and technical data and information deemed to be of continuing reference value. NASA's counterpart of peer-reviewed formal professional papers but has less stringent limitations on manuscript length and extent of graphic presentations.

- TECHNICAL MEMORANDUM. Scientific and technical findings that are preliminary or of specialized interest, e.g., quick release reports, working papers, and bibliographies that contain minimal annotation. Does not contain extensive analysis.

- CONTRACTOR REPORT. Scientific and technical findings by NASA-sponsored contractors and grantees.

- CONFERENCE PUBLICATION. Collected papers from scientific and technical conferences, symposia, seminars, or other meetings sponsored or cosponsored by NASA.

- SPECIAL PUBLICATION. Scientific, technical, or historical information from NASA programs, projects, and mission, often concerned with subjects having substantial public interest.

- TECHNICAL TRANSLATION. English-language translations of foreign scientific and technical material pertinent to NASA's mission.

Specialized services that complement the STI Program Office's diverse offerings include creating custom thesauri, building customized databases, organizing and publishing research results…even providing videos.

For more information about the NASA STI Program Office, see the following:

- Access the NASA STI program home page at <http://www.sti.nasa.gov>

- E-mail your question via the Internet to <help@sti.nasa.gov>

- Phone the NASA STI Help Desk at 757–864–9658

- Write to:
  NASA STI Information Desk
  Mail Stop 148
  NASA Langley Research Center
  Hampton, VA 23681–2199, USA

NASA/TM—2018–219863

Mechanisms of Oxide Formation in the Self-Reacting Friction Stir Weld Process

J.A. Schneider
The University of Alabama in Huntsville, Huntsville, Alabama

J.P. Norris and P. Chen
Jacobs ESSST, Marshall Space Flight Center, Huntsville, Alabama

A.C. Nunes, Jr.
Marshall Space Flight Center, Huntsville, Alabama

National Aeronautics and
Space Administration

Marshall Space Flight Center • Huntsville, Alabama 35812

August 2018

TRADEMARKS

Available from:

NASA STI Information Desk
Mail Stop 148
NASA Langley Research Center
Hampton, VA 23681–2199, USA
757–864–9658

TABLE OF CONTENTS

LIST OF FIGURES

LIST OF FIGURES (Continued)

LIST OF FIGURES (Continued)

LIST OF TABLES

LIST OF ACRONYMS AND SYMBOLS

Al	aluminum
Al_2O_3	aluminum oxide
AS	advancing side
CFSW	conventional friction stir welding
Cu	copper
EDS	energy dispersive x-ray spectroscopy
FSW	friction stir welding
Li	lithium
LN_2	liquid nitrogen (–195 °C)
Mg	magnesium
MSFC	Marshall Space Flight Center
ROD	residual oxide defect
RT	room temperature (23 °C)
RS	retreating side
SEM	scanning electron microscopy
SRFSW	self-reacting friction stir welding
STEM	scanning transmission electron microscopy
TEM	transmission electron microscope
UTS	ultimate tensile strength

NOMENCLATURE

b	base
E	elastic modulus
g	gap between faying surfaces
h	height or panel thickness
I	moment of intertia
V	travel velocity of friction stir welding tool
y_C	critical gap between faying surfaces
δ	thickness of shear zone
σ	tensile stress
τ	shear stress
ω	angular velocity of friction stir welding tool

TECHNICAL MEMORANDUM

MECHANISMS OF OXIDE FORMATION IN THE SELF-REACTING FRICTION STIR WELD PROCESS

1. INTRODUCTION

The initial objective of this study was to evaluate the effect of an extended delay time between preweld cleaning and the completion of a self-reacting friction stir welding (SRFSW) process on the resulting quality of various thickness panels of AA2219-T87. The current NASA standard specifies no more than a 48 hr delay between preweld cleaning and actual welding. The concern is whether increasing the cleaning delay time results in development of the residual oxide defect (ROD) in SRFSW. This concern emanates from the possibility of increased time correlating with increased oxide layer thickness on the faying surfaces. Oxide content on the faying surfaces has been reported to correlate with the occurrence of the ROD which reduces mechanical properties. When the SRFSW process was first adopted by the NASA Marshall Space Flight Center (MSFC), unexpected low tensile values that resulted were attributed to oxides within the weld that appeared to follow the former faying surface contours. Mitigation of the ROD was achieved through a combination of modifications to the processing parameters, tool designs, and incorporation of a weld seam offset.

Two operations are involved in preweld cleaning: the first is removal of oil and grease, and the second is removal of surface oxides. In arc welding, improper cleaning of the faying surfaces of aluminum welded joints can increase the sensitivity toward development of defects. As the aluminum is locally melted, these contaminants contribute toward the development of porosity, inclusions, entrapped oxides, and other discontinuities which can degrade the strength of the weld joint. For weldment of large structures, the weld joint is typically cleaned, fit-up, and tack welded prior to the final full penetration welding pass. Because of the stringent joint fit-up requirements for mismatch and peaking for launch vehicle structures, the joint fit-up can sometimes contribute to lengthy delays between cleaning and tack welding, especially for circumferential weld joints on large diameter components.

When the conventional friction stir welding (CFSW) process was introduced at the NASA MSFC, there was no procedure for cleaning prior to the solid-state joining process. As the process expanded to include SRFSW, preparation of the faying, crown, and root surfaces were implemented to overcome the ROD.[1,2] Although the solid-state process is not expected to reach temperatures high enough for dissociation of the native oxide layer, concern remained regarding the redeposition of the native oxide layer within the stir zone. NASA has previously established the allowable time at 48 hr between preweld cleaning and a SRFSW process. The effect of potential contamination resulting from an extended delay to 188 hr was subsequently evaluated for SRFSWs using tensile testing and metallographic imaging. Tensile specimens were tested at room temperature (RT), and at cryogenic conditions of liquid nitrogen (LN_2) and liquid hydrogen. No detrimental effect on weld quality, as determined by weld strength, was reported for cleaning delays of 48, 120, 168, 240 or 288 hr.

While no trends were established in this study, which extended the delay from 48 to 188 hr, there were a few outliers in terms of ultimate tensile strength (UTS). According to M. Fisher's 2014 Boeing Company Memo no. EYBF-MAF-14-029, all outliers were above the minimum acceptance criteria, but out of family with respect to the average values. As the robustness and reliability of any process ultimately depends on the average values as well as the outliers, an understanding of the cause of these outliers will ultimately improve the process. This report examines those outliers and their possible causes.

2. BACKGROUND

2.1 Weld Preparation

Weld quality is influenced by the preparation and cleanliness of the surfaces being joined. Two operations are involved in preweld cleaning: the first removes oil and grease, and the second removes oxides. On large structures, delays are historically encountered between the time a joint is preweld cleaned and when it undergoes a full penetration weld. These delays raise concerns due to the extended exposure to environmental moisture and debris which could potentially contaminate the previously cleaned surfaces.

2.2 Aluminum and Its Alloys

Aluminum alloys are used extensively in the aeronautical and astronautical industries due to their high strength-to-weight ratio, corrosion resistance, and cryogenic compatibility. Of particular interest to NASA is the 2xxx series aluminum alloys which are strengthened by precipitates formed during appropriate heat treatments. The solid-state joining technique of friction stir welding (FSW) can result in improved properties of weldments of these 2xxx series alloys. Although the solid-state joining technique eliminates many of the metallurgical issues associated with conventional fusion welding, there continues to be concern regarding the redeposition of the native oxide present on the faying surface and its subsequent impact on material properties. Since the joining temperatures are much lower in a solid-state joining process than fusion welding, it is not expected that the aluminum oxide (Al_2O_3) will reach the melting temperature of 2,072 °C.

2.3 Friction Stir Welding

Early weld trials at the NASA MSFC were conducted on aluminum alloys AA2219 and AA2195 for implementation into the production schedule for the space shuttle external tanks. The CFSW process was originally introduced at the NASA MSFC for fabrication of a lightweight version of the space shuttle external tank out of a new aluminum alloy, AA2195, which proved difficult to weld by fusion processes. In CFSW, a large axial compression force was required on the tool, which had to be reacted against a heavy anvil incorporated into the weld fixture. A later version of the FSW process, called the SRFSW process, was patented in 2004.[3] The modified tool design eliminated the requirement for a large axial force by splitting the tool in two and pulling crown and root shoulders together to balance the axial compression within the tool and substitute a squeeze for an unbalanced axial force.

In addition to eliminating the requirement for a bulky backing anvil, the temperatures in a SRFSW were also higher, allowing for a faster travel velocity. The higher temperatures are believed to be due to the additional heat input path through the second shoulder and the removal of the large heat sink represented by the backing anvil.

As the NASA MSFC moved to the SRFSW process, a defect became apparent, especially when joining the AA2195, an aluminum (Al)-lithium (Li)-copper (Cu) alloy. The defect was correlated with oxide remains within the weld nugget, which could weaken the mechanical strength. Because of the link between the oxides and the former faying surface, this defect was referred to as a "lazy S," "lazy Z," joint line defect, or ROD. Other studies in the literature report similar characteristics, but refer to them as kissing bond defects.[4] Since this is not a detectable defect using standard nondestructive inspection techniques (such as phased array ultrasonics), many studies have been undertaken to understand why this defect occurs primarily with SRFSWs, and in particular AA2195, and how best to mitigate its occurrence.

An extensive study undertaken by NASA and Lockheed Martin, and documented in the SDS 6103 SRFSW Reference Book, examined prewelding cleaning methods, preweld cleaning durations, and preweld cleaning durations for ROD mitigation. The panels used were 0.81 cm (0.32 in) thick and focused on material combinations of AA2195/AA2195 and AA2219/AA2195. The weld parameters used for the AA2195/AA2195 panels were 150 RPM/406 mmpm (16 ipm) and a crown/root force of 0.6/13.3 kN (125/3,000 lb_f). For the AA2219/AA2195 weld panels, the parameters were 150 RPM/356 mmpm (14 ipm) and a crown/root force of 0.6/13.3 kN (125/3,000 lb_f). In the preweld cleaning method, the AA2195 showed a greater sensitivity to weld quality as affected by the presence of ROD. In Section 3.2 of the Reference Book, a cleaning procedure was established in which an alcohol wipe was applied, followed by either a wire brush or manual scrape on the crown and root joint surfaces, and a final draw file across the abutting edges. This provided a more severe mechanical removal of the surface oxides on the AA2195 by using manual scraping and eliminated a final alcohol wipe of the surface.

After establishing the preweld cleaning procedure, a follow-on study looked at the effect of delays in completing the weld within 14 to 20 days for the bimetallic joint of AA2219/AA2195. The SRFSW parameters were modified slightly in this study using a lower tool rotation of 140 RPM/356 mmpm (14 ipm). ROD was considered prevalent in all SRFSWs in this study based on reduced average tensile strength and data scatter. It was in this study that the observation was made regarding the possibility for oxide to form on the root side faying surfaces during a continuous FSW tack weld.

The study also documents efforts taken to mitigate the ROD which found that a centerline offset of 0.48 cm (0.19 in) for the weld tool was most effective in eliminating the ROD. The process parameters were not documented in this study. Cleaning delays of 11 and 16 days were evaluated in SRFSWs which used a skip tack process.

Although the SRFSW process provided flexibility in joining complex geometries, it was not readily adaptable to the production of tack welds. Tack welds could be made using the CFSW process (which required heavy fixtures) or by gas tungsten arc welding. Studies were undertaken to ensure that the localized melting of a partial penetration tack weld did not promote oxidation, such as ROD, that would be detrimental to the weld strength.[5] These studies were undertaken in AA2195-T8 panels of 0.65 cm (0.257 in) and 0.83 cm (0.327 in) thickness. This study varied the tack weld parameters in a stitch pattern and found no detrimental effect of a fusion tack weld on the resulting strength of a SRFSW, as evidenced by tensile testing at RT. Effects of both the incorporation of a fusion tack as well as typical strength variations along the length of the panel were evaluated. The SRFSW parameters for the 0.65 cm (0.257 in)-thick panels were 225 RPM, 381 mmpm (15 ipm), and 10.7 kN (2400 $\mathrm{lb_f}$) pinch force whereas the SRFSW parameters for the 0.83 cm (0.327 in)-thick panels were 150 RPM, 381 mmpm (15 ipm), and 17.8 kN (4000 $\mathrm{lb_f}$) pinch force. Influence of the tool offset was included in the study by considering a retreating side (RS) tool offset of 0 cm (0 in) and 0.15 cm (0.06 in). Although the study concluded that the use of fusion tack welds was not detrimental to the SRFSW strength, there was more variation noted in the 0.65 cm (0.257 in)-thick panels which were welded at higher tool rotations than the 0.83 cm (0.327 in)-panels.[5]

2.4 Joint Line Defect or Residual Oxide Defect

Various reports on the CFSW process have been published in the literature regarding the behavior of the initial oxide layer on the base material surface and its effect on the resulting mechanical properties of FSW aluminum alloys. If these oxides are not consumed or adequately dispersed in the FSW, they can remain in the weld nugget and result in a typical joint line remnant defect as shown in figure 1. The joint line remnant typically comprises an array of oxides that can be seen from the macrostructure at very low magnifications. Joint line remnant defect is believed to result from the presence of oxide film on the surface of the workpiece due to poor cleaning. The joint line remnant is also referred to as the kissing bond, lazy S, lazy Z, or ROD.[4,6–9]

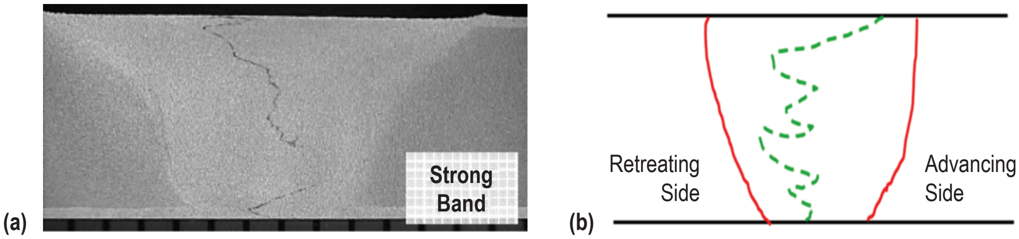

Figure 1. Metallographic image (a) of a CFSW showing the typical Lazy S, or ROD, feature and (b) illustration of the pattern.

Models of the FSW process have promoted the understanding that the joint is achieved by shear strain arising from rotation of the welding tool along the pin surface.[10–13] Thus this shear strain is believed to break up the native aluminum oxide (Al_2O_3) layer, generating oxide-free surfaces around the rotating pin. However, if the oxide particles are of sufficient size, they may flow collectively during the FSW process and accumulate in the lazy S feature reported. Since the amount of flow increase varies from the root to the crown in FSW, most remaining oxide particles are reported near the root region.[14] As the pin is offset to the RS, the oxide particles are expected to decrease in size to the point of no detection[10] due to the increasing shear strain.

Krishnan[1] commented on the report of oxides in a manuscript by Larsson[2] and speculated that oxides could form along the layers of metal as they are sheared and consolidated in the wake of an aluminum alloy FSW. Speculation was made that at some point in time, purge gases might be required to avoid oxidation. Since then, various studies have investigated the effect of the joint line remnant on mechanical properties and have found no detrimental effect for the CFSW process.[4,8,9,14] Only one study found a degradation of properties, and that was in tensile testing of AA2219-O that was subjected to a post weld heat treatment. However, from the images presented, the weldment also experienced abnormal grain growth which was not discussed as a contributing factor.[9]

Most studies indicate that the joint line remnant can be eliminated by proper selection of FSW parameters of tool rotation, travel, and tilt.[4,8,15–18] In many studies, the remnant line was only visible when the workpiece surfaces were anodized prior to the FSW.[9,10] An interesting observation was made in a study by Li et al on FSW of AA2219-T6 in which coarsened particles of precipitated Al_2Cu phase were found around a kissing bond defect as evidenced by scanning electron microscopy (SEM)/electron discharge machining within the stir zone.[4] The presence of these coarsened particles suggested that the primary reason for a kissing-bond formation was not due to insufficient heat input, but rather a heat input that was too high, as earlier speculated.

These studies would indicate that the observation of a joint line remnant is not an indication of inadequate cleaning or extended delay between cleaning and full penetration welding of the aluminum workpieces surfaces, but rather an indication of nonoptimized FSW parameters. This observation is based on the weld offset used in SRFSW which was used to eliminate the occurrence of remnant line defect. By offsetting the tool to the RS of the weld seam, the faying surface is brought in from the advancing side (AS) which increases the time (fraction of tool rotation) under high temperature and pressure.[10] Figure 2 illustrates sealing up and oxidation of a weld seam as it follows a streamline around a FSW pin shown in a plan view. The weld seam is shown entering the shear surface (slip line) in which bounding metal clings to the FSW pin as a streamline. The material travels from right to left while the tool rotates in a counter-clockwise direction. The seam acquires surface oxide before it is sealed up, i.e. welded. A hypothetical surface oxidation within the shear "surface," actually a thin extended region, is shown. The seam continues along its streamline to emerge behind the tool as a welded seam remnant incorporating oxide.

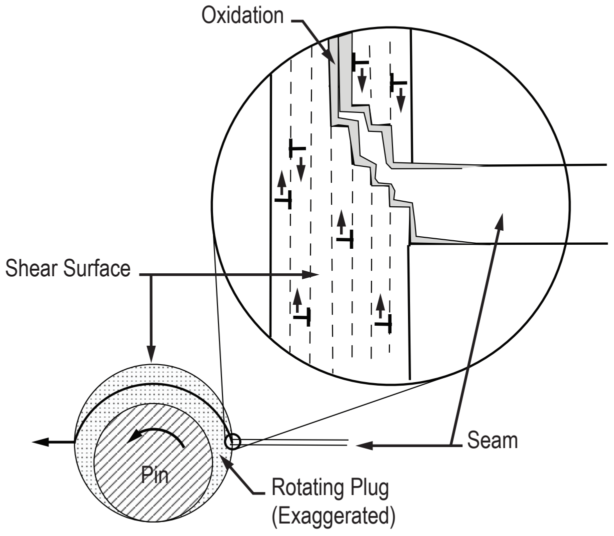

Figure 2. Sealing and oxidation of a weld seam as it follows a streamline around a FSW pin shown in a plan view.

Assuming that the flow velocity increases linearly from weld metal to rotating plug over the thickness δ of the shear surface, which exists at a radius r from the center of the weld nugget, its derivative with respect to time is illustrated in figure 3 and given in equation 1:

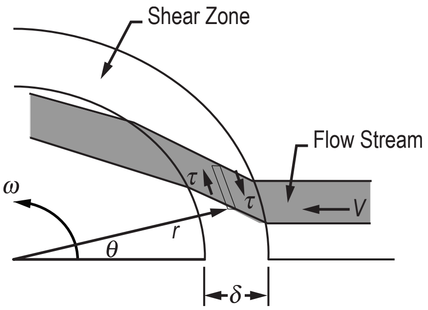

Figure 3. Details of flow stream velocity as material crosses the shear zone.

$$\frac{d}{dt}\left(r\frac{d\theta}{dt}\right)=r\omega\left(\frac{V\cos\theta}{\delta}\right) \quad . \tag{1}$$

If r can be taken as constant, then equation 1 can be presented as equation 2:

$$\frac{d^2\theta}{dt^2}=\frac{V\omega}{\delta}\cos\theta \quad , \tag{2}$$

and if $\cos\theta$ changes very little during the period of interest, it can be approximated by equation 3:

$$\theta-\theta_0 \sim \frac{1}{2}\left(\frac{V\omega}{\delta}\cos\theta_0\right)t^2 \quad . \tag{3}$$

Thus the distance y traversed across the shear surface is given in equation 4:

$$y \sim V\cos\theta_0 t \quad , \tag{4}$$

so that the gap closure is given by equation 5:

$$r\left(\theta-\theta_0\right) \sim \frac{\delta}{2}\left(\frac{r\omega}{V\cos\theta_0}\right)\left(\frac{y}{\delta}\right)^2 \quad . \tag{5}$$

Given a gap Δg between two streamlines entering the shear surface, the faying surfaces maintain a closing distance Δy. At some critical distance Δy_C the gap effectively closes. The gap closure distance $r(\theta - \theta_0)_C$ along the shear surface is estimated by equation 6:

$$r\left(\theta-\theta_0\right)_C \sim \frac{\delta}{2}\left(\frac{V\cos\theta_0}{r\omega}\right)\left(\frac{\Delta g}{\Delta y_C}\right)^2 \; . \tag{6}$$

In figure 2, the gap closure distance shown is on the order of the shear surface thickness, a few thousandths of an inch (0.0254 mm or 0.001 in). In actuality, although the gap closure configuration doubtless plays a significant role in determining the state of oxidation of the seam residue, it has not been studied as far as the authors of this work are aware. In addition, the gap width can also be altered by the weld parameters.

2.5 Aluminum Oxidation Rate

A film of Al_2O_3 is always present on the surface of aluminum and its alloys. Based on the Pilling-Bedworth Ratio, this oxidation layer is predicted to be protective. Due to its parabolic growth rate, the oxide growth occurs within seconds and is self-limiting in thickness. This oxidation growth rate can be accelerated by the presence of high humidity, temperature, or moisture.[19] Most theories and studies regarding the oxidation of solid aluminum consider the first monolayer of oxidation to be virtually instantaneous, and only dependent on the arrival rate of oxygen. This monolayer develops into an amorphous layer where it may transform into one of the crystalline phases of Al_2O_3.[20] The rate of oxidation is dependent upon both the oxygen arrival rate and the rate of diffusion through the existing oxide layer. Earlier studies published the stable oxide layer at a thickness of 2–3 nm.[21–23] Later studies found that the crystalline structure and orientation affected the oxide thickness, expanding the range from 0.5 nm[20,24] to 4 nm.[25] The maximum thickness reported in the literature is reported to be 20 nm at temperatures up to 300 °C.[26]

The rate of oxidation for aluminum is noted to be influenced by both temperature and moisture. At low temperatures (<300 °C), the oxide film growth rate is considered to be very fast initially, followed by an abrupt and drastic reduction to virtually zero, or self-limiting, within less than 250 s.[26–27] The kinetics of aluminum oxidation follows a parabolic law in the temperature range 350–475 °C and reaches an equilibrium thickness rapidly. At higher temperatures, the oxidation follows a linear law and can reach a greater thickness.[26] The kinetic rate is reduced if the initial surface oxide is crystalline rather than amorphous. The native oxide layer is amorphous, but can crystallize at elevated temperatures. Thus, oxidation rates at elevated temperatures (>500 °C) are reported to stabilize in thickness at approximately 200 nm.[26–27]

The effect of alloying elements on the oxidation rate has been studied for molten aluminum.[28] These studies found that the oxidation rate increases with the addition of sodium, lithium, calcium, and magnesium (Mg).[29,30] Alloying effects on the oxidation rates in solid metal has been evaluated in electroplating and anodizing studies in which the Mg content correlated with an increase in oxidation rate.[31] A contrasting 2004 NASA study by R. Boothe and K. Bennett ("Aluminum oxidation rate study") reported the oxidation behavior for a series of solid aluminum alloys in which a delay was reported in the onset of oxidation after grit blasting that correlated with the Li content. No further elemental or structural analysis was undertaken to characterize the oxide formed. A summary of effects is given in table 1.

Table 1. Effects of alloying elements on oxidation rates.

AA	Delay in Oxidation Onset (hr)	Li Content (%)	Mg Content (%)	Cr Content (%)	Reference
AA2024	NA*	–	1.2–1.8	<0.1	
AA6061	NA*	–	1.2–1.8	0.04–0.35	
AA7075	5	0.001–0.003	2.1–2.9	0.18–0.28	39
AA2219	5	0.001–0.003	<0.02	–	39
AA2195	10	0.8–1.2	0.25–0.8	–	39
AA2099	18	1.6–2.0	0.1–0.5	–	39

* NA = not available.

In a study by Sato, et al.[14] applying transmission electron microscopy (TEM), the particles along the remnant line were found to be amorphous Al_2O_3, suggesting that the oxide had not been subjected to high temperatures for any length of time. Because of the amorphous nature, the oxides were attributed to native oxide films on the aluminum prior to FSW. In contrast, Li et al.[4] reported the presence of coarsened particles of precipitated Al_2Cu phase in the region around a kissing bond defect. Thus, this study suggested higher temperatures occurred resulting in the coarsening of the Cu-rich particles. No information was presented on the oxide phases within the remnant region.

Based on the literature, the concern regarding initial oxidation films on the workpiece would not be expected to be affected by delays between cleaning and performing the SRFSW. A stable oxide layer would not be expected to increase as a function of additional time at RT. As a stable oxide layer of 1–2 nm is noted to form within 250 s, any further delay after cleaning would not be expected to result in thicker oxide layers. Even in the presence of high humidity, a stable layer is still expected to form within seconds. However, the noted change in oxidization rates at temperatures greater than 500 °C suggests that the remnant line oxides may come not from the native oxides on the surface of the aluminum workpiece, but from the FSW process. Thus, the occurrence of ROD may correlate with FSW temperature either due to weld parameters and/or the higher temperature of the SRFSW process. Systematic studies have found the tool rotation to have the most influence on the resulting weld properties.[32] Other studies have shown the effect of varying temperature from small changes in the tool rotation on the resulting weld microstructure.[33]

3. EXPERIMENTAL PROCEDURE

3.1 Weld Schedule

All SRFSWs evaluated in this study were conducted on the ESAB LEGIO™ weld system at the NASA MSFC in Building 4755. Butt welds were made in 76×15 cm (30×6 in) panels of 2219-T87/2219-T87. A CFSW stitch tack was made on all panels using the parameters listed in table 2. These SRFSWs were produced with a 168 hr delay between cleaning and the full penetration weld.

Table 2. CFSW tack parameters used in study.

Panel Thickness (cm)	Spindle Rotation (RPM)	Travel Speed (mmpm)	Plunge Force (kN)
0.95	550	178	17.8
1.27	700	127	13.3
1.59	900	127	5.6

The weld parameters are summarized in table 3 along with the logged torque for the shoulder and the pin. The LEGIO configuration independently drives the upper shoulder and the pin and lower shoulder. Thus, there is a torque measurement associated with the upper shoulder, called spindle torque, and another torque measurement associated with the pin and lower shoulder, called the pin torque. Because of the combined drive of the pin and the lower shoulder, the pin torque has a higher value. Note the LEGIO software header lists the torque in units of lb. Based on the range of torques measured, the logged data is most likely in foot-pounds.

Table 3. SRFSW schedule.

Panel ID	Panel Thickness (cm)	Upper Shoulder Force (kN)	Pin/Lower Shoulder Force (kN)	RPM	Travel (mmpm)	Spindle Torque (N-m)	Pin Torque (N-m)
P13	0.95	14.7	16	195	304.80	113	147
P14	0.95	14.7	16	195	304.80	107	154
P15	0.95	14.7	16	195	304.80	108	154
P16	0.95	19.1	20	205	304.80	118	143
P17	0.95	19.1	20	205	304.80	125	140
P18	0.95	19.1	20	205	304.80	124	137
P01	1.27	15.6	18	130	177.80	143	265

Table 3. SRFSW schedule (Continued).

Panel ID	Panel Thickness (cm)	Upper Shoulder Force (kN)	Pin/Lower Shoulder Force (kN)	RPM	Travel (mmpm)	Spindle Torque (N-m)	Pin Torque (N-m)
P02	1.27	15.6	18	130	177.80	143	262
P03	1.27	15.6	18	130	177.80	145	260
P04	1.27	20.0	22	150	177.80	162	215
P05	1.27	20.0	22	150	177.80	163	213
P06	1.27	20.0	22	150	177.80	164	215
P07	1.59	16.9	19	140	177.80	170	292
P08	1.59	16.9	19	140	177.80	161	295
P09	1.59	16.9	19	140	177.80	154	301
P10	1.59	20.0	22	155	177.80	179	250
P11	1.59	20.0	22	155	177.80	162	262
P12	1.59	20.0	22	155	177.80	168	259

3.2 Mechanical Properties

Mechanical properties of the welds were evaluated in tensile tests at the Mechanical Materials Test Facility at the NASA MSFC. Standard tensile specimens were machined transverse to the weld as shown in figure 4. A total of 6 RT specimens were tested for each of the 6 panels per material thickness. Two specimens per panel were run with each specimen completely submerged in LN_2 and soaked 5 minutes prior to test start.

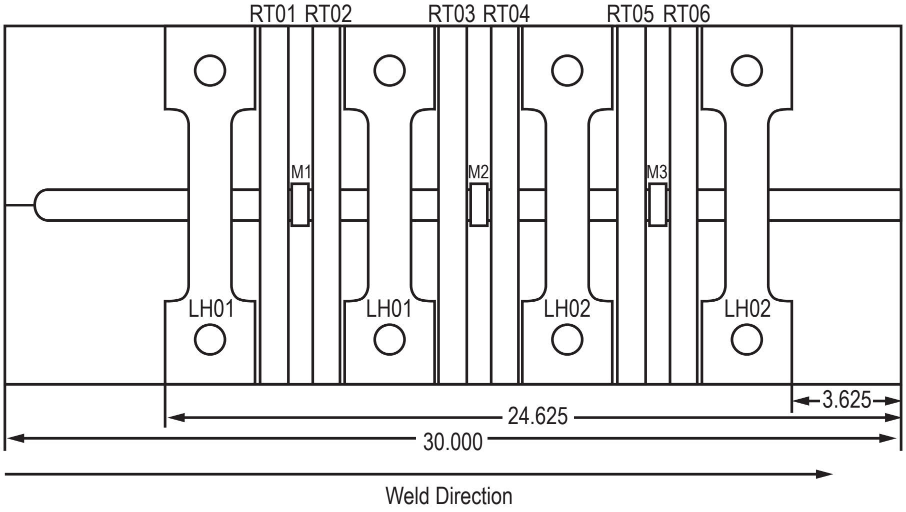

Figure 4. Orientation and geometry of tensile specimens. (Note: Dimensions are in inches).

All tensile tests were conducted on a screw-driven mechanical actuator which used a linear variable differential transformer for displacement feedback. Stress measurements were based on loads obtained from an 89 kN load cell and specimen dimension measurements. Strain measurements were obtained from a 2.5 cm extensometer calibrated to 50% strain. All tests were run in displacement control at a constant crosshead velocity of 0.13 cm/min. Stress measurements were calculated using the load cell data and specimen cross sectional area. Strain measurements were obtained directly from the use of extensometers.

3.3 Metallography

Metallographic specimens were removed from the panels as shown by M1, M2, and M3 locations in figure 4 along with specimens from selected tensile tests. The specimens were mounted in a phenolic, then ground, polished, and etched using Keller's reagent to reveal the macrostructure. Photographs were taken of all transverse sections in addition to higher magnification optical images using a Nikon® D1 camera. Higher magnification images were taken using a Hitachi S-3700N SEM with tungsten emitter. Elemental maps were made using an Oxford X-Max EDS.

Selected specimens were prepared for TEM. A Hitachi NB-5000 Dual-Beam FIB system was used at the Oak Ridge National Laboratory. This allowed site specific foils to be removed. The foils were imaged in a Hitachi HF-3300 field-emission gun TEM with a cold cathode emitter at an accelerating voltage of 300 kV. In the scanning transmission electron microscopy (STEM) mode, a high-angle annular dark-field detector was used to obtain elemental mapping based on Z contrast.

4. RESULTS

4.1 Mechanical Properties

A more detailed summary of the ultimate tensile strength data for various delay times in cleaning is documented elsewhere. The data summarized in this report considers both the UTS and percentage of elongation to failure. Figures 5, 6, and 7 present the mechanical property data for the panels measuring 0.95 cm (0.375 in), 1.27 cm (0.500 in), and 1.59 cm (0.625 in) in thickness, respectively. These figures compare the data for cold versus hot weld parameters for the panels tested at RT and at LN_2 temperature. With the exception of figure 6 for the 1.59 cm (0.625 in)-thick panel no. 10, little variation is noted in the mechanical properties at either test temperature.

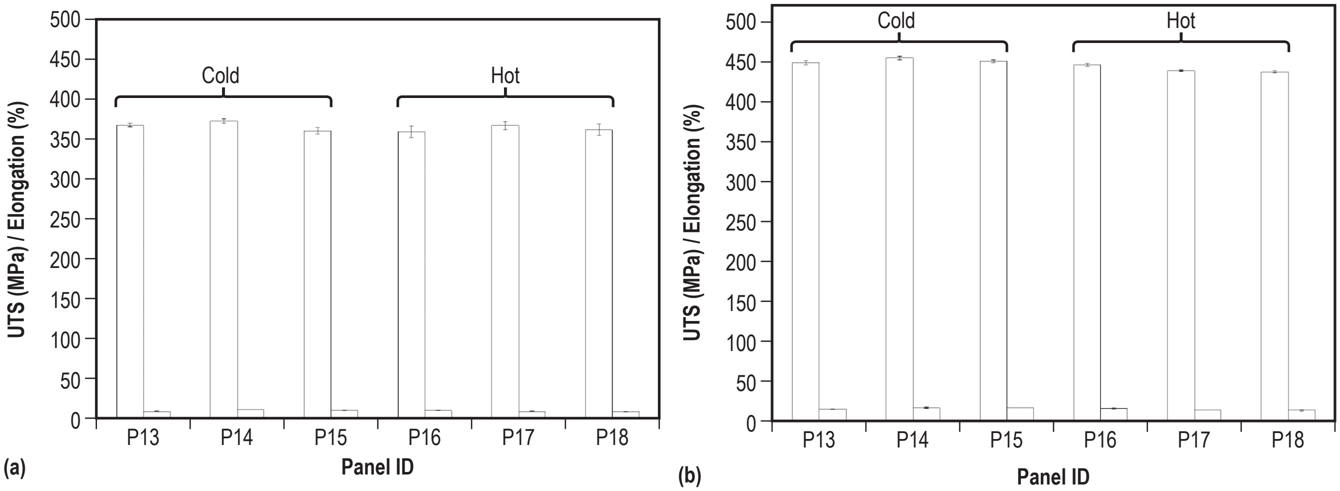

Figure 5. Summary of mechanical properties of the 0.95 cm (0.375 in)-thick SRFSW panels tested at (a) RT and (b) LN_2.

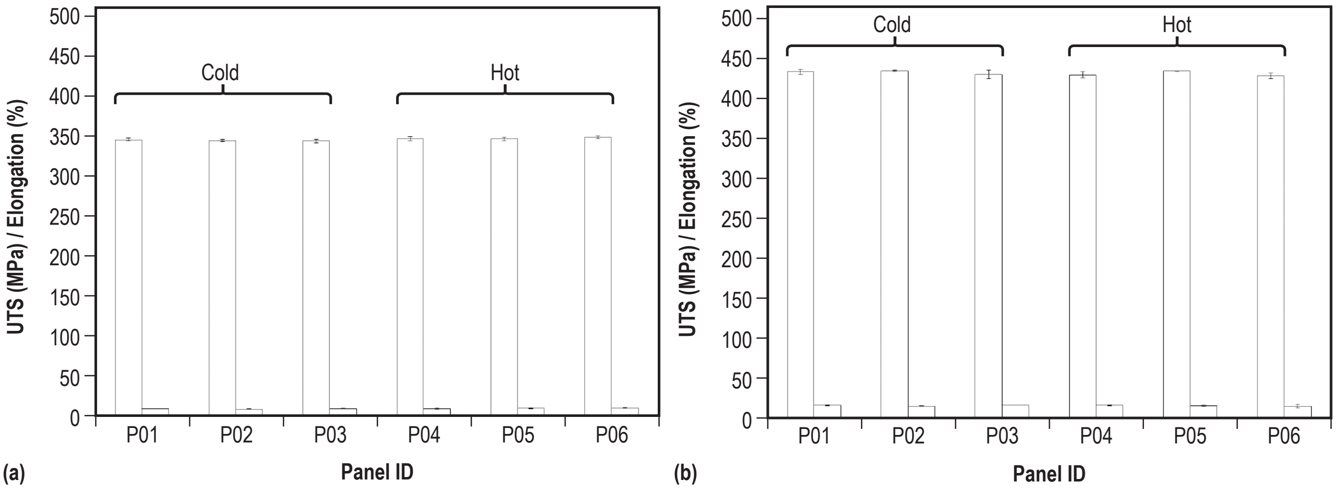

Figure 6. Summary of mechanical properties of the 1.27 cm (0.500 in)-thick SRFSW panels tested at (a) RT and (b) LN_2.

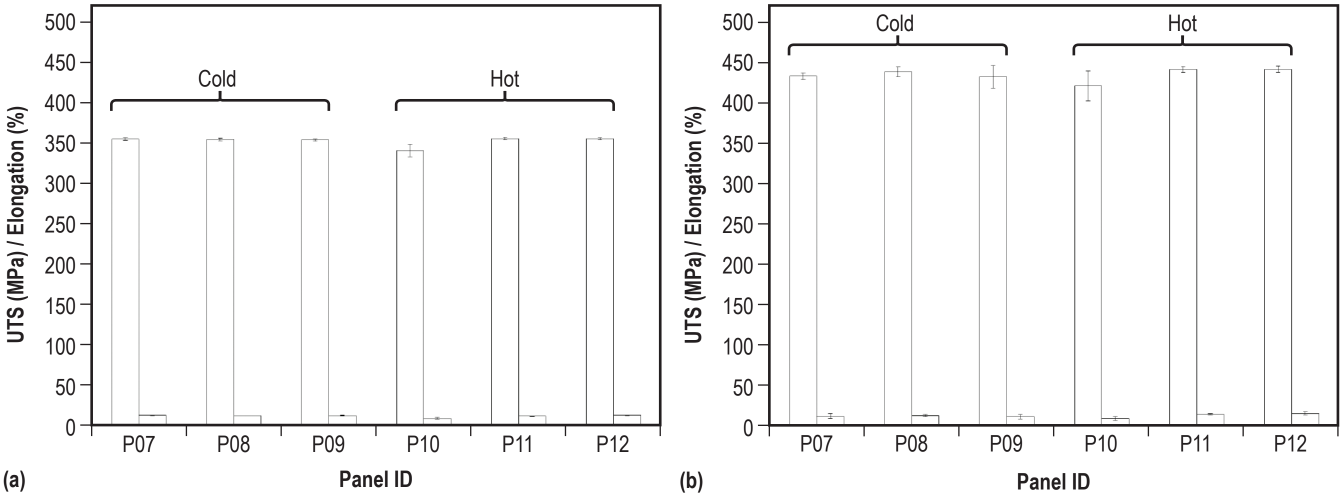

Figure 7. Summary of mechanical properties of the 1.59 cm (0.625 in)-thick SRFSW panels tested at (a) RT and (b) LN_2.

Although all mechanical property data was in compliance with the acceptance criteria described in M. Fisher's Boeing Company memo mentioned in the Introduction section of this paper, representative specimens were selected on the basis of nominal and lowest properties to probe the cause of the outliers (documented in P-S. Chen's "Weld microstructure analysis for 2219-T8/2219/T8 SR FSW" 2015 presentation). The specimens metallurgically evaluated are listed in table 4.

Table 4. Selected specimens for metallographic inspection.

Specimen ID	Weld Parameter	Individual UTS (MPa)	Panel Average and Standard Deviation for UTS	Individual Elongation (%)	Panel Average and Standard Deviation for Elongation	Fracture Location
375-P14-RT01	Cold	374.0	372.7 ± 2.9	10.66	10.51 ± 0.23	RS
375-P17-RT05	Hot	371.4	366.9 ± 5.2	8.77	8.46 ± 0.16	AS
375-P18-RT04	Hot	355.9	361.8 ± 7.1	7.7	8.11 ± 0.29	AS
375-P18-LN01	Hot	436.7	437.7 ± 1.3	11.98	12.53 ± 0.77	AS/nugget
375-P15-M03	Cold	–	360.4 ± 0.4	–	9.60 ± 0.36	RS
500-P02-RT05	Cold	344.7	345.7 ± 1.4	9.97	9.64 ± 0.21	RS
500-P06-RT02	Hot	349.0	349.2 ± 1.7	11.59	11.22 ± 0.61	AS
500-P03-RT02	Cold	345.2	344.9 ± 2.3	9.7	10.03 ± 0.3	RS
500-P05-RT04	Hot	343.8	347.5 ± 2.1	9.86	10.52 ± 0.52	AS
625-P07-RT06	Cold	352.7	354.3 ± 1.7	11.61	11.46 ± 0.39	RS
625-P10-RT03	Hot	338.0	339.8 ± 7.5	7.69	7.92 ± 1.12	AS

4.2 Metallographic Studies

4.2.1 Optical Microscopy

Representative images from samples listed in table 4 are shown in this section to document the appearance of panels with the nominal and the lowest properties.

Figure 8 shows a high strength weld using the cold parameters, and a crack on the RS where it failed. In comparison, figure 9 shows a high strength weld joined at the hot parameters which failed on the AS. While the mechanical properties are within acceptance criteria and little scatter is noted in the data, these are not considered to be typical failures of robust welds.

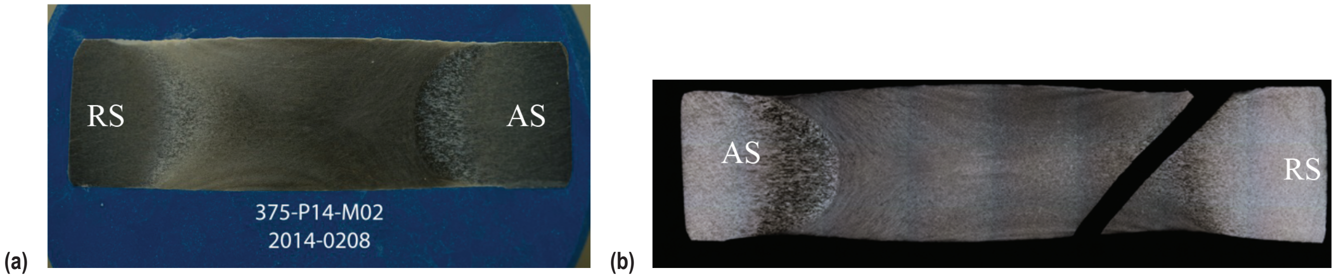

Figure 8. Panel no. 375-P14: (a) Metallograph for the M02 specimen in the panel and (b) the corresponding break observed for tensile specimen RT01.

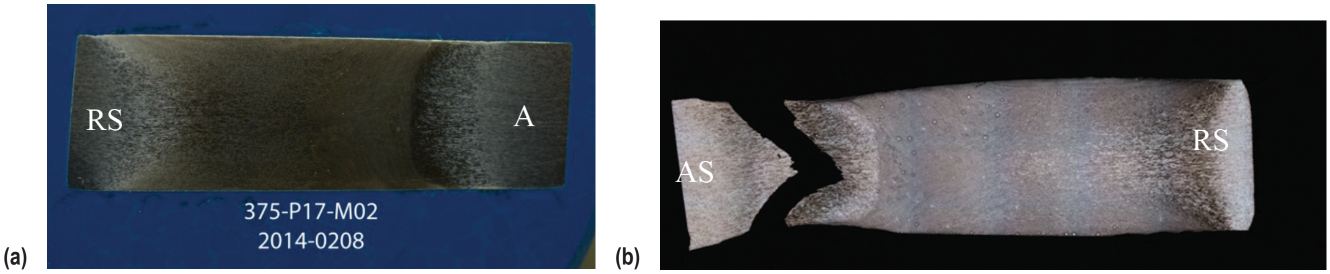

Figure 9. Panel no. 375-P17: (a) Metallograph for the M02 specimen in the panel and (b) the corresponding break observed in tensile specimen RT05.

Figure 10 shows the metallograph for the lowest strength specimen joined at the hot parameters which also fractured along the AS. At LN_2 temperatures, the fracture is more pronounced through the weld nugget. Figure 11 shows some higher magnification images which capture the line feature in the nugget region. Figure 10(b) demonstrates that this line is not a crack, and further shows appearances of abnormally small grains and thickened grain boundaries.

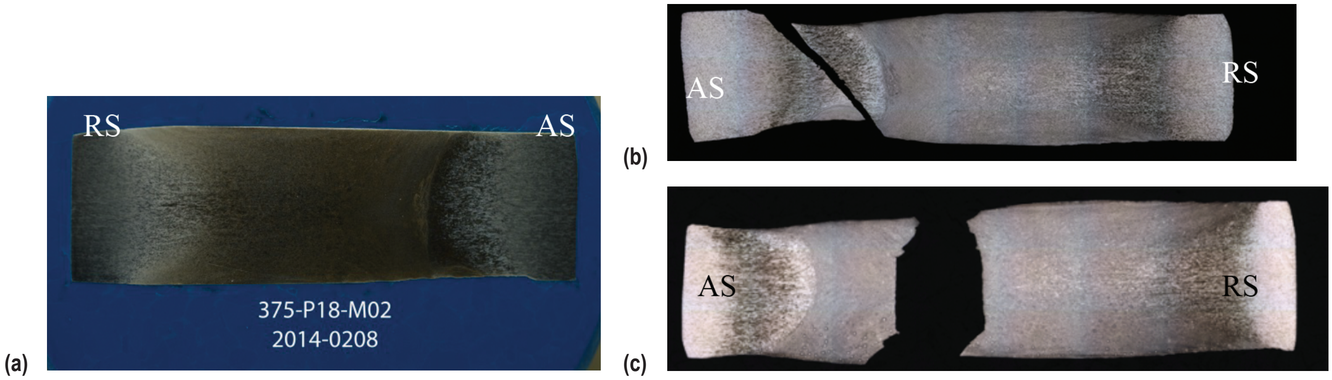

Figure 10. Panel no. 375-P18: (a) Metallograph for the M02 specimen in the panel, (b) corresponding RT break in tensile specimen RT04, and (c) LN_2 tensile specimen LN01.

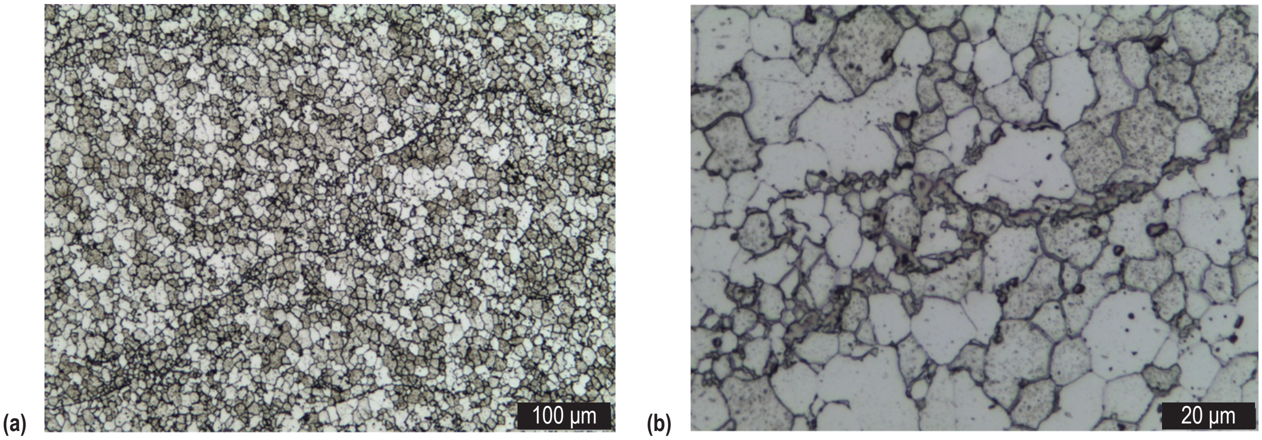

Figure 11. SRFSW no. 375-P18-M01 (a) closeup of line feature and (b) associated fine grain region.

This line feature was fairly common in all the 0.95 cm (0.375 in)-thick SRFSWs as evidenced by figure 12, which was also joined at the hot parameters. The appearance of these lines in the 0.95 cm (0.375 in)-thick SRFSW did not correlate with lower strength or ductility.

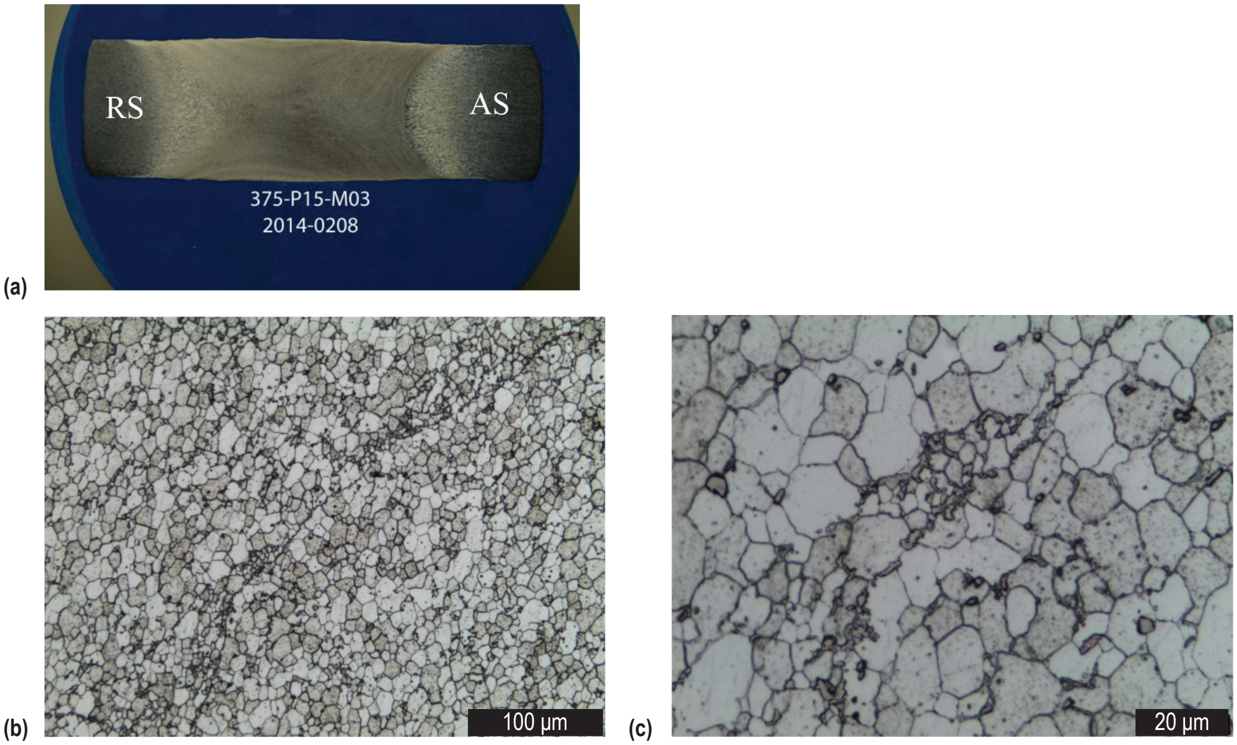

Figure 12. Panel no. 375-P15: (a) Metallograph for the M03 specimen in the panel, (b) closeup of line feature, and (c) associated grain details of line feature.

Similar characteristics were observed in the high and low property specimens for the 1.27 cm (0.5 in)-thick SRFSW as shown in figures 13 and 14, respectively. Figure 15 shows a higher magnification metallurgical image of the low property weld microstructure in which the line feature can be observed.

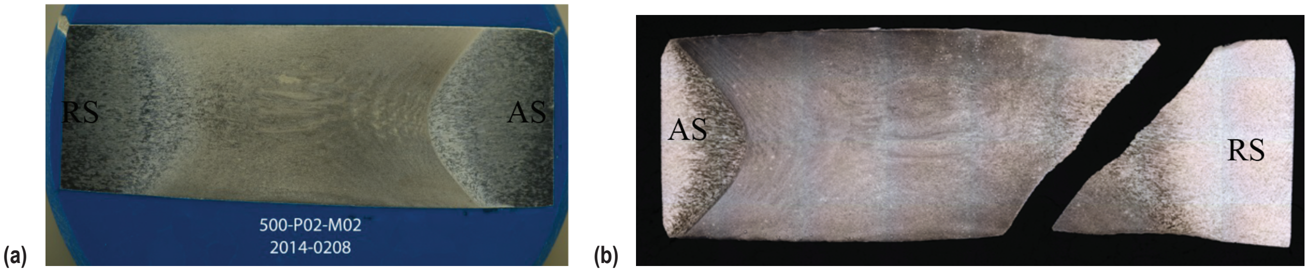

Figure 13. Panel no. 500-P02: (a) Metallograph for the M02 specimen in the panel and (b) corresponding fracture location in tensile specimen RT05.

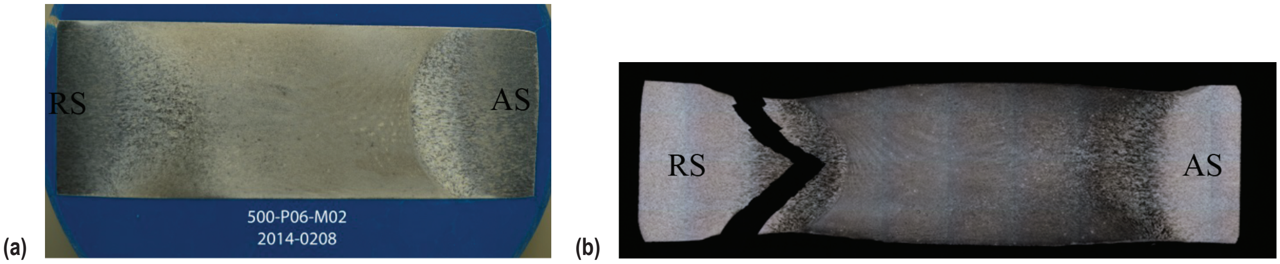

Figure 14. Panel no. 500-P06: (a) Metallograph for the M02 specimen in the panel and (b) corresponding fracture location in tensile specimen RT02.

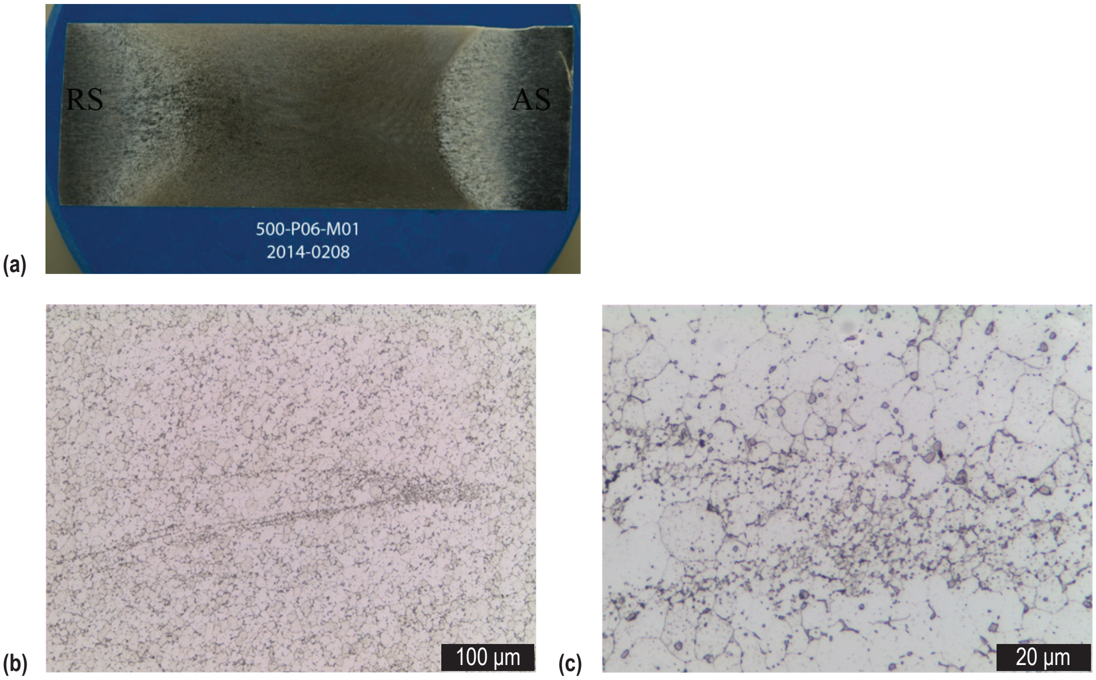

Figure 15. Panel no. 500-P06: (a) Metallograph for the M01 specimen in the panel, (b) closeup of line feature in weld nugget, and (c) small grain region associated with the line feature

The largest mechanical property variation, although still within the acceptance criteria, was observed in the 1.59 cm (0.625 in)-thick SRFSWs. Figure 16 shows a nominal property specimen which failed on the RS. The line indications were also observed within this weld nugget as shown in figure 17. A closeup of this region in figure 17(b) shows a region of very fine grains which give rise to this dark line appearance in figure 17(a).

Figure 16. Fracture location in specimen no. 625-P07-RT06.

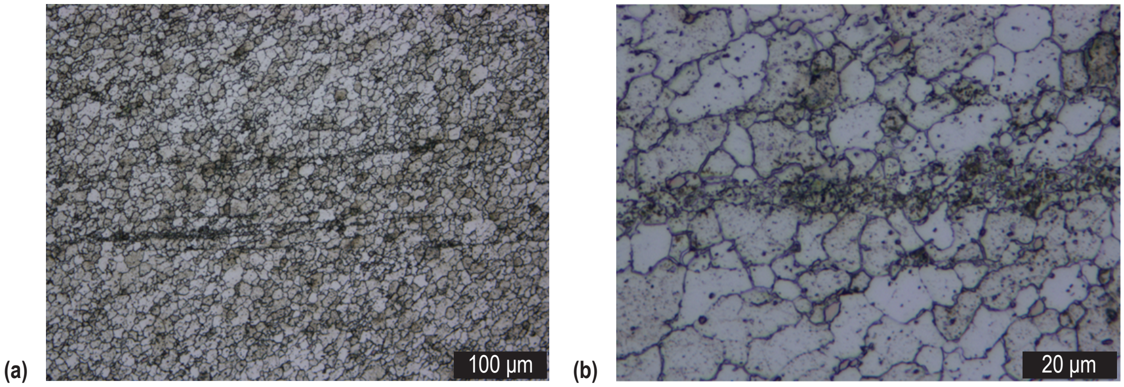

Figure 17. SRFSW no. 625-P07-RT06: (a) closeup of line feature and (b) associated fine grain features.

Figure 18 is a macrograph of the lowest strength SRFSW in the 1.59 cm (0.625 in) panels. The fracture path is on the AS and extends through the weld nugget, but in a more irregular and jagged pattern. Also noted within figure 17 is evidence of tears on the AS root surface which follow the metal flow lines. However, since this metallographic specimen was taken after a tension test to failure, it is possible that the line features observed broke open under tension. Therefore it is inconclusive to state that these tears contributed to the lower strength, but may be an indication of the nature of the line features. If these line features are a brittle phase, then they become a failure initiation site.

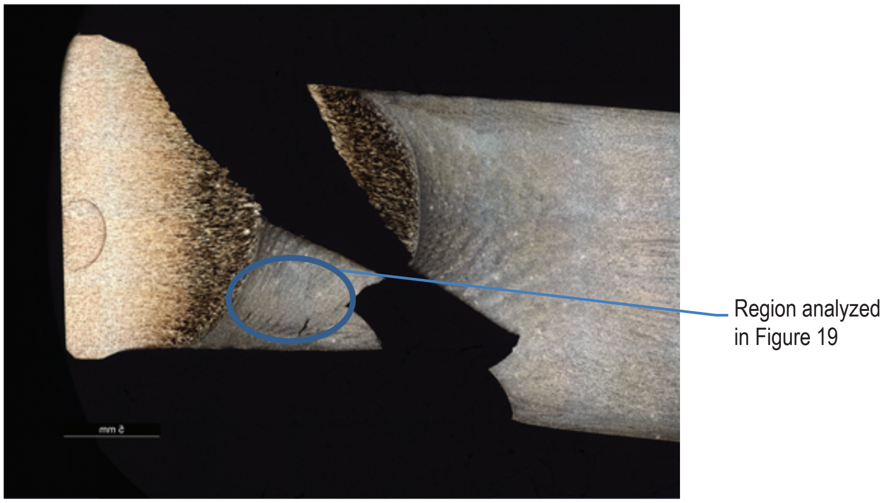

Figure 18. Fracture location for SRFSW no. 625-P10-RT03.

Figure 19 shows a series of images from the nugget of P10 SRFSW tensile specimen which contains the line features observed in the other panel thickness. But, these images also capture regions where tears have formed. Figure 20 shows one of these tears and also shows evidence of porosity in the region adjacent to the tear.

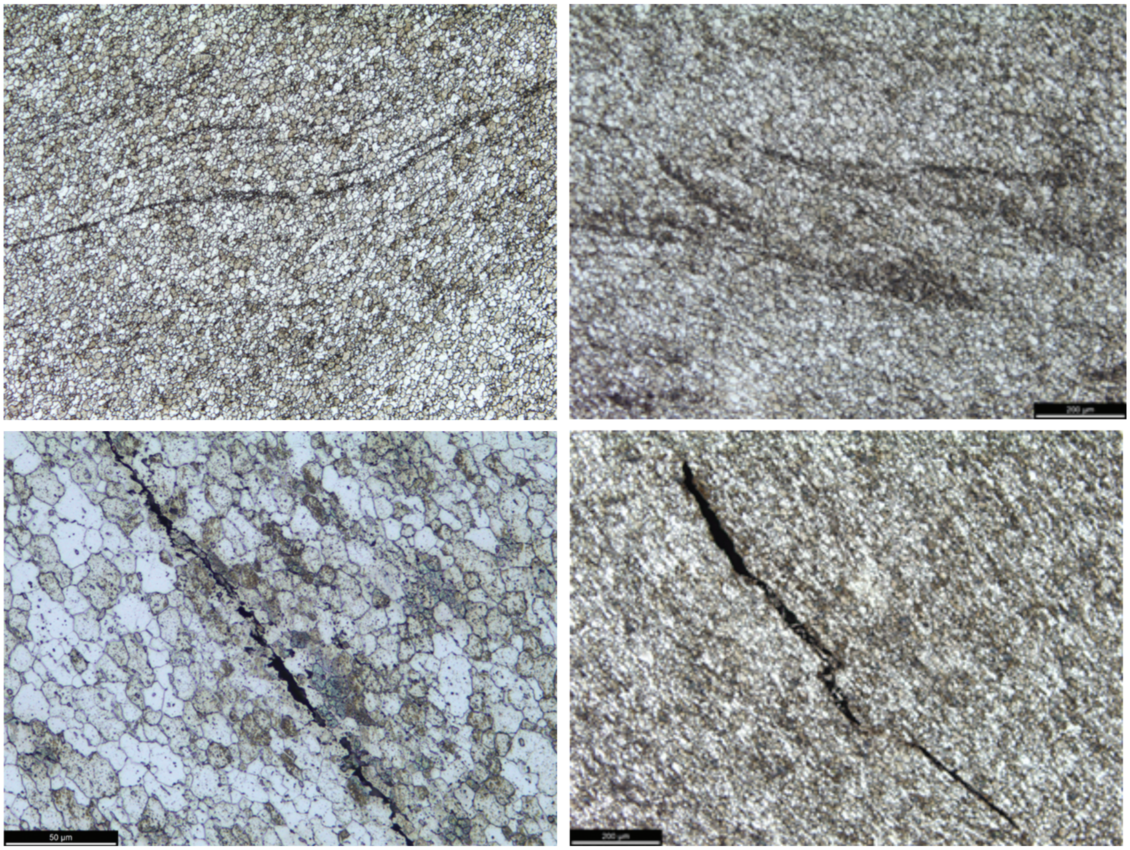

Figure 19. SRFSW no. 625-P10-RT03 showing closeup of regions with line features and the presence of hot tears.

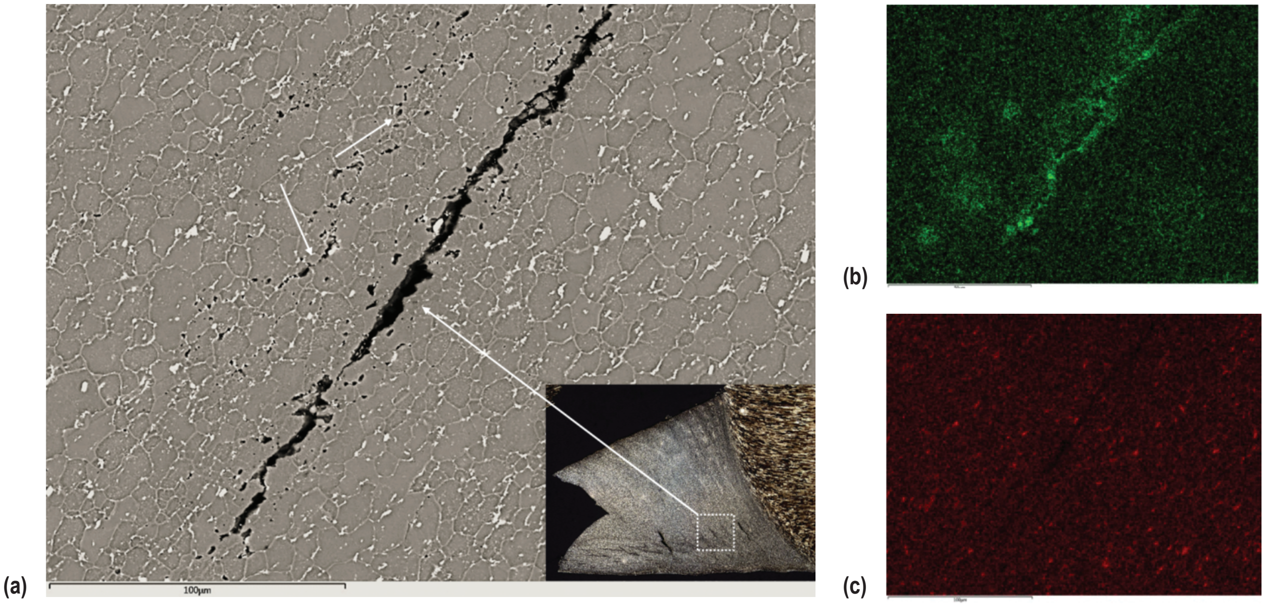

Figure 20. Tear in no. 625-P10-RT03: (a) Closeup of tear, and noted porosity in adjacent regions along with EDS maps for (b) oxygen and (c) copper.

4.2.2 SEM/EDS

To investigate the elemental composition of the line features observed, SEM/EDS was used. An SEM image is shown in figure 21 of one of the banded regions in figure 16. The figures shows the location of regions where EDS was used to determine the elemental composition. The EDS analysis is summarized in table 5. The large light particles, spectrum 5 and 6, in addition to spectrum 3 and 4, exhibit Al and Cu contents close to the binary eutectic composition of 66.8/33.2 wt%.

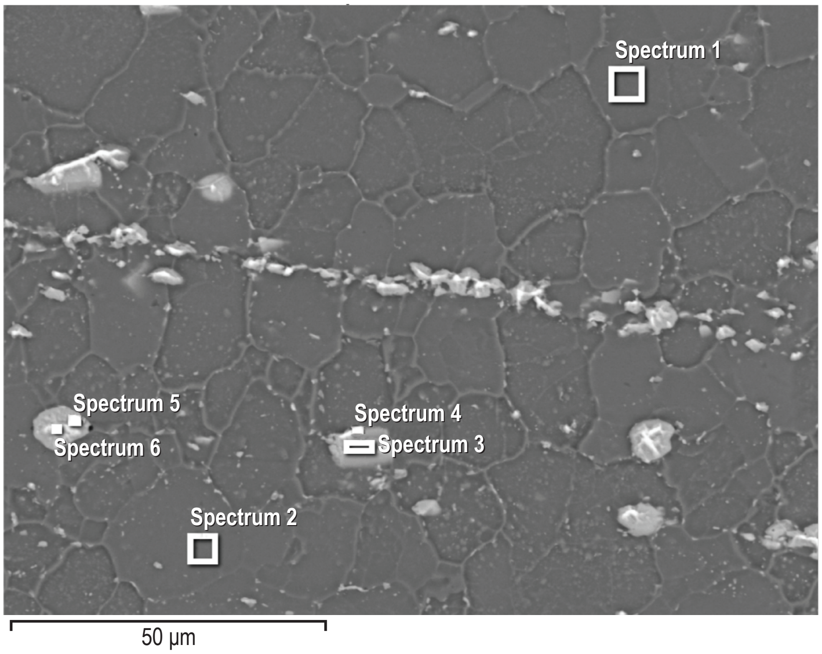

Figure 21. SEM overview of a banded region shown in figure 16.

Table 5. EDS analysis of regions within figure 21 in weight percent.

	Element (wt %)							
Label	C	O	Al	S	Mn	Fe	Cu	Sb
Spectrum 1	4.41	0.51	88.38	–	0.26	–	6.43	–
Spectrum 2	4.41	0.51	87.95	–	0.34	–	6.80	–
Spectrum 3	5.31	2.12	61.19	–	1.85	5.56	23.97	–
Spectrum 4	6.60	1.17	47.50	–	0.25	0.35	42.01	2.13
Spectrum 5	5.19	0.45	59.91	–	–	–	34.45	–
Spectrum 6	5.18	0.77	45.76	0.24	–	–	45.36	2.70

4.2.3 TEM/STEM/HAADF

TEM foils were prepared from specimen no. 625-07-RT06, shown in figure 16, to obtain higher magnification information on the structure of the light and dark regions observed. To identify these regions, carbon tape was used to highlight the dark versus light features as shown in figure 22. Note figure 15 is a bright field image and figure 20 is a dark field image, thus the light and dark are reversed. Three TEM foils were removed, one from the light grain region, one from the dark grain region, and one near the AS root shoulder.

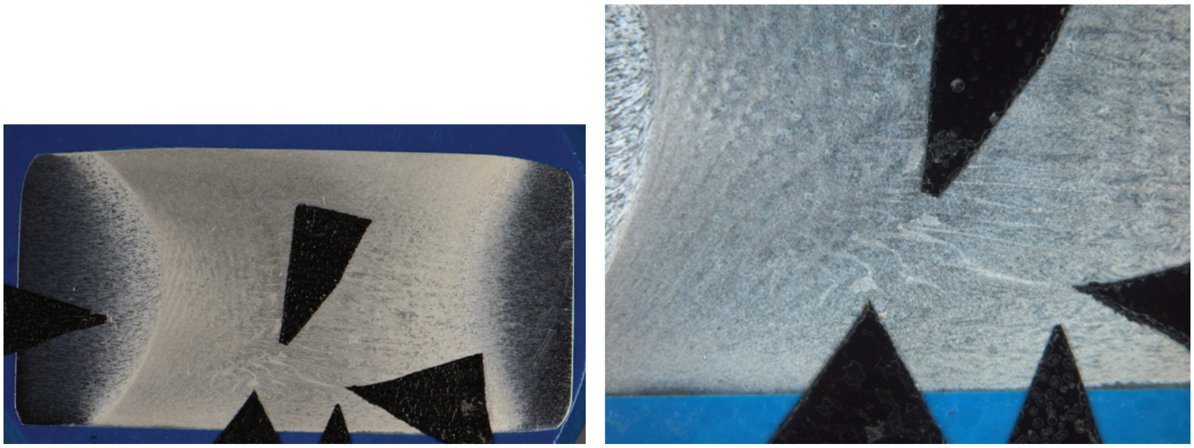

Figure 22. Highlighted region of dark versus light grains from specimen shown in figure 16.

Figure 23 shows an overview of the TEM foil removed from the light grain region. Observed are large Cu-rich grains, especially along the grain boundaries. Little evidence is observed of the expected strengthening precipitates within the grain interior. A high magnification image of the Cu-rich grain boundary phase from figure 23 is shown in figure 24. The image shows a lamellar structure, expected in the eutectic Al-Cu phase. In the binary Al-Cu system, the eutectic phase has a melting temperature of 548 °C.

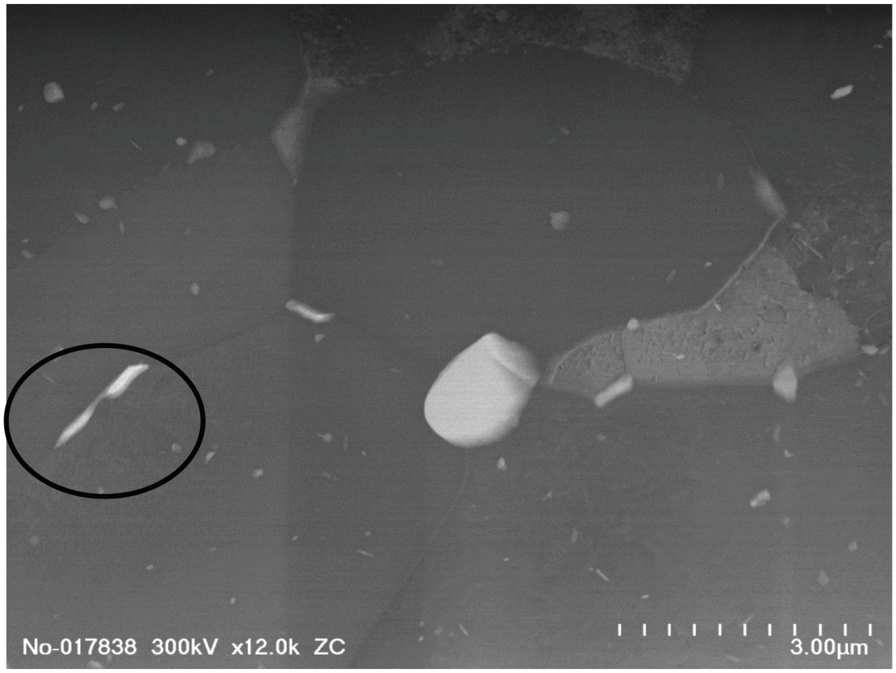

Figure 23. Overview of a light grain region from sample no. 625-P07-RT06.

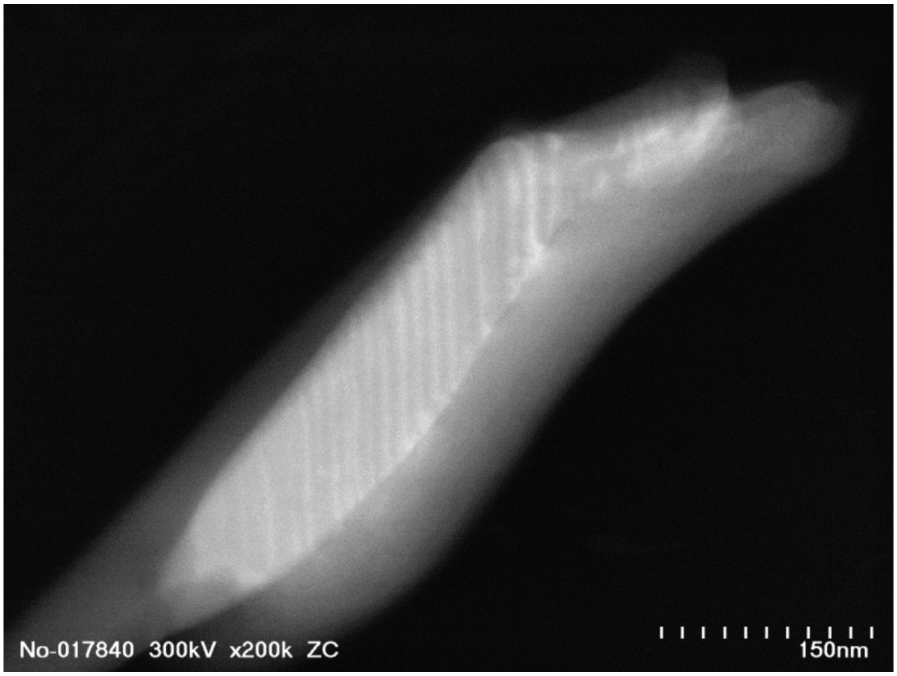

Figure 24. Closeup of a Cu-rich phase along a grain boundary showing a lamellar structure.

Figure 25 shows an overview of the TEM foil removed from the dark grain region. Here finer precipitates are observed along the grain boundary, but with larger Cu-rich phases within the grain. No lamellar structure is observed in these Cu-rich particles within the grain interiors.

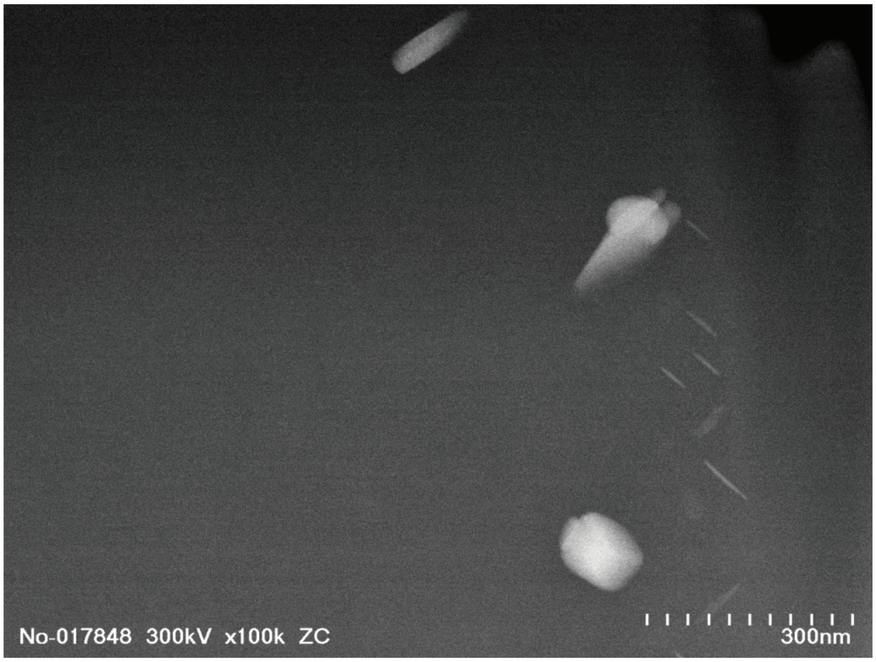

Figure 25. Overview of a dark grain region from sample no. 625-P07-RT06.

Figure 26 shows images from the TEM foil removed from the AS crown surface. In contrast to the other regions, a mixed precipitate distribution is observed corresponding to different stages of coarsening. Cu-rich particles are also observed along the grain boundary (figure 26(c)). A closeup image of the grain boundary phase shown in figure 26(c) is shown in figure 27. Lamellar details are also present, similar to figure 24.

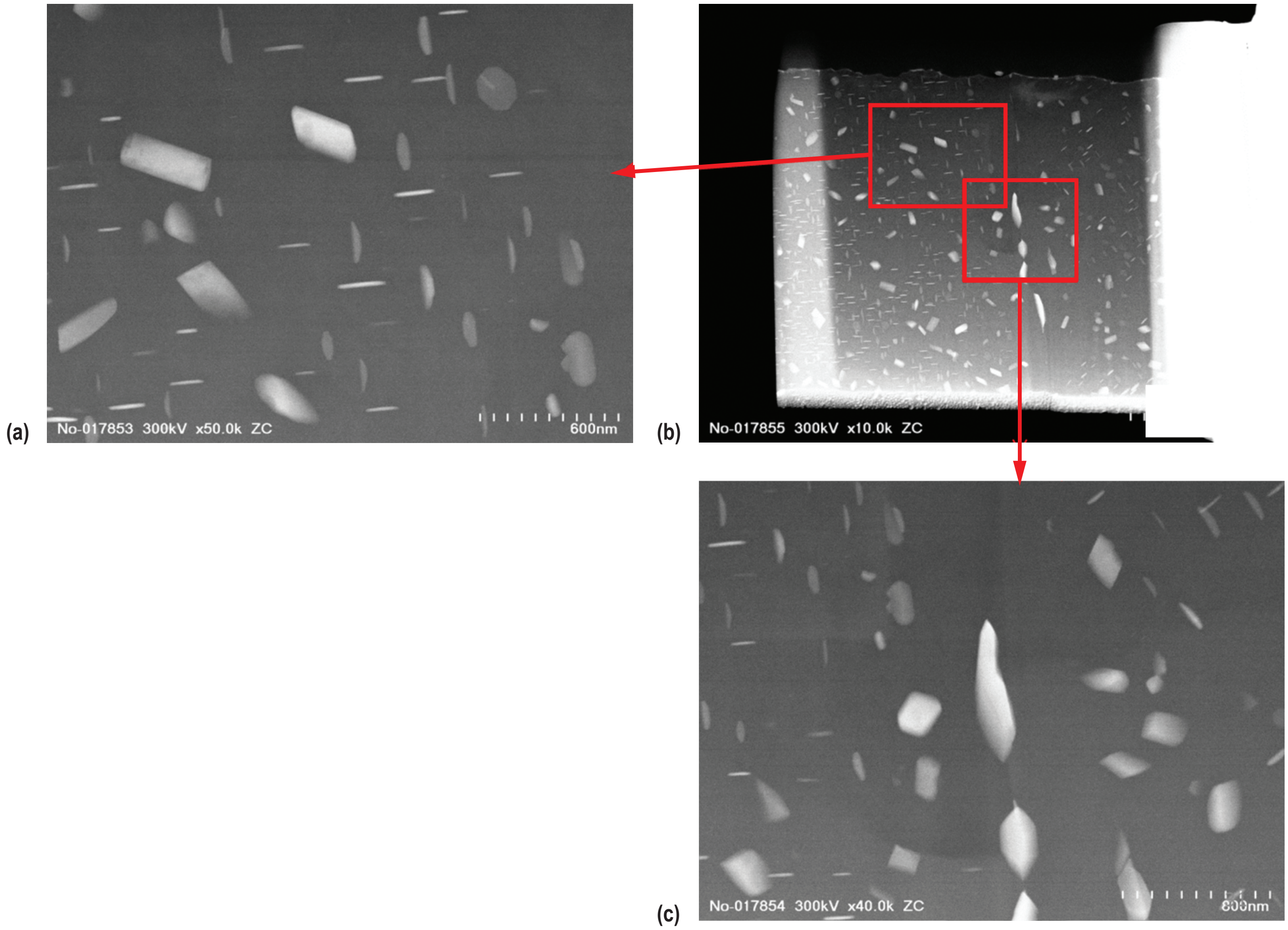

Figure 26. Images of TEM foil removed from the AS crown surface showing (a) a closeup of mixed precipitate sizes within a grain, (b) an overview of the foil, and (c) an enlarged view of the elongated Cu-rich particles along the grain boundary.

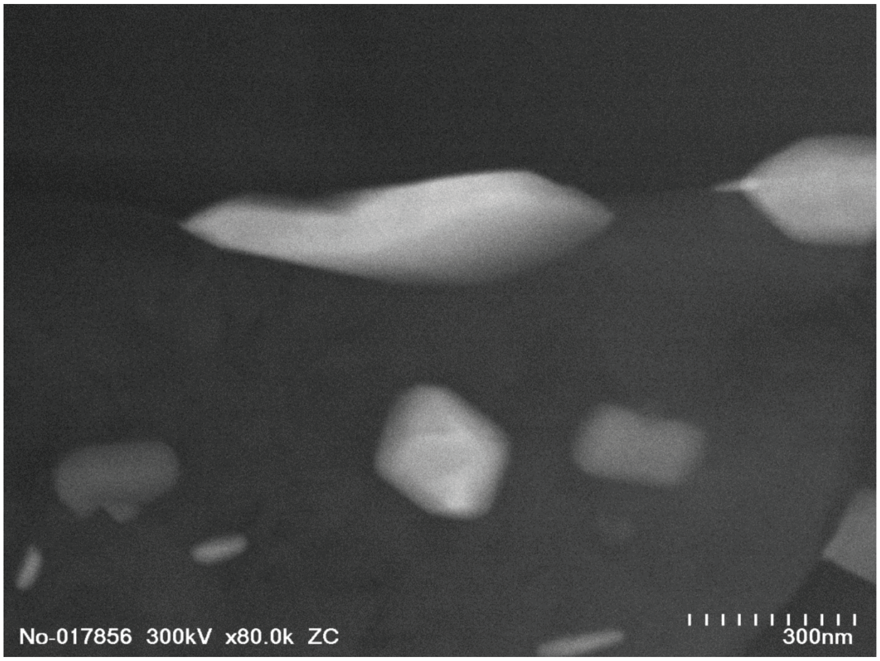

Figure 27. Closeup of the Cu-rich grain boundary phase from figure 26(c).

5. DISCUSSION

In reviewing the tensile test data, there is some variation within the tensile strength and elongation to failure. Although all values were within acceptable ranges, there were outliers, or out of family values, for several test specimens. Outliers suggest that something is occurring within the weld specimens that may appear somewhat random in occurrence, but could compromise the robustness of the process if not understood and mitigated.

Although not all specimens broke on the RS of the weld nugget, there was no correlation of tensile break with the tensile results. Line features were observed in all SRFSWs, but did not appear to be kissing type bonds. Microstructural analysis of the weld zone showed an increasing tendency for regions of oxides associated with refined grains as the weld panel thickness increased to 1.59 cm (0.625 in). Additionally, in the 1.59 cm (0.625 in)-thick weld panels, tears were observed in post tensile test specimens in these refined grain regions, which appear to follow the metal flow lines in the FSW process.

The temperature of the weld panel has been most strongly correlated with the tool rotation. The amount of torque required to form a FSW is related to temperature; higher temperatures reduce the torque. Considering these relationships, it appears that the 5% increase in tool rotation for the 0.95 cm (0.375 in)-thick panel did not appreciably change the temperature, as the measured torque remains fairly constant. In contrast, increasing the tool rotation over 10% does correspond to a decrease in torque for both the 1.27 cm (0.5 in)- and 1.59 cm (0.625 in)-thick workpieces.

An observation, illustrated by figures 28 and 29, is that gaps form in advance of a FSW. These gaps can be exaggerated, as shown in figure 27, as the weld panels increase in thickness. This gap can be explained by one of two mechanisms: the unbalanced pinch loading, or the increased pressure as the pin is plunged into the panel.

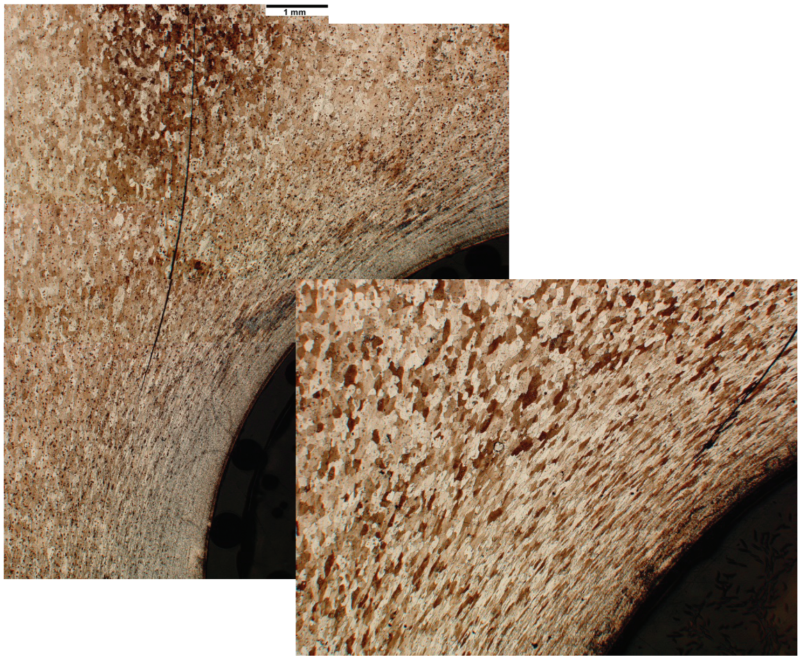

Figure 28. Gap in 0.64 cm (0.25 in)-thick weld panels at end of the CFSW.

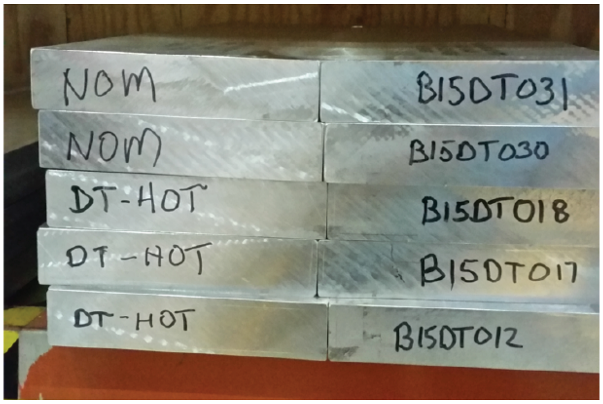

Figure 29. Gap in 3.2 cm (1.25 in)-thick weld panel after tack welding.

A gap in advance of the weld tool can form as the force differential between the pin/root shoulder force and the crown shoulder force results in a load on the panels at the location of the joint as illustrated in figure 30. As the clamps are approximately 3.2 cm (1.25 in) from the weld seam, the AS and RS side of the weld seam can be considered as a cantilever beam illustrated in figure 31. The deflection of the cantilever beam assembly is given by y in equation 7:

$$y=-\frac{PL^3}{3EI} \tag{7}$$

where

I = the moment of inertia given in equation 8
h = panel thickness
b = 1.

$$I=\frac{1}{12}bh^3 \quad . \tag{8}$$

The corresponding angle formed as the beam deflects is illustrated in figure 31, and given as θ in equation 9:

$$\theta=\frac{PL^2}{2EI} \tag{9}$$

The resulting load (P) on the workpiece is the pinch force, or delta between the applied crown shoulder force and the pin/root shoulder force, and L is the distance from the weld seam to the clamp. E = 69 GPa (10 x 10^6 psi), the elastic modulus of Al.

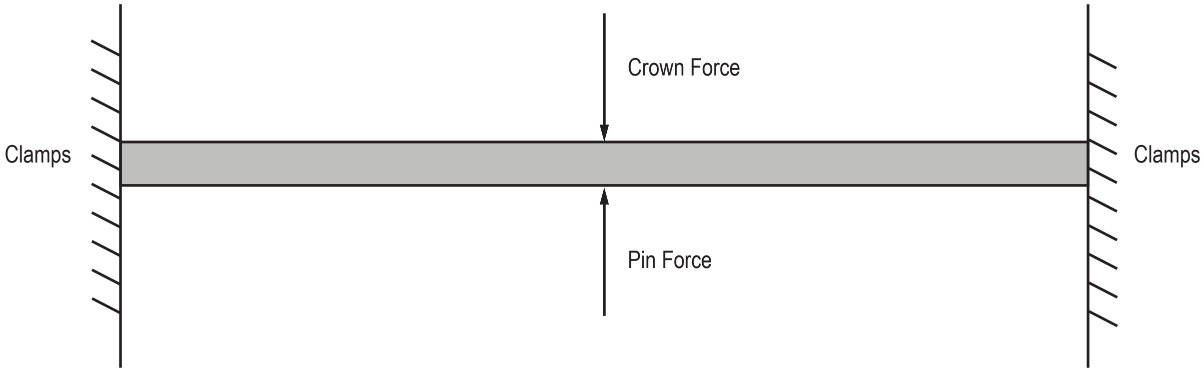

Figure 30. Schematic of workpiece as a simple cantilevered beam in bending.

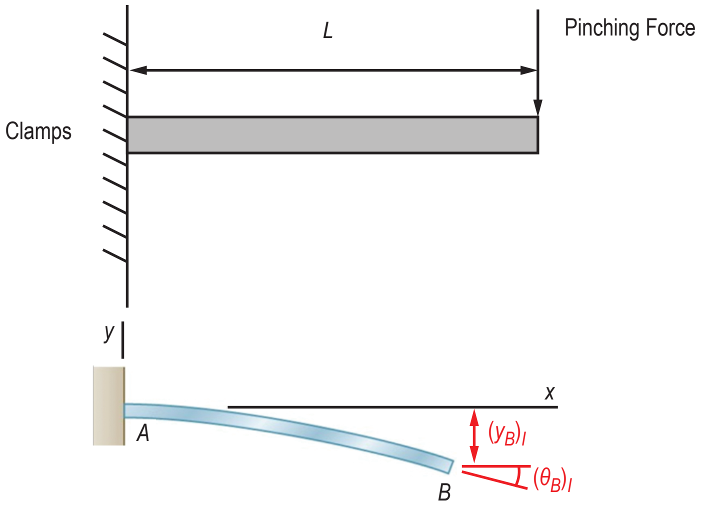

Figure 31. Beam deflection expected from resulting pinching force applied at weld seam.

Estimations of the deflection and resulting gap thickness are summarized in table 6. Although the increasing thickness of the workpiece increases the resistance to deformation, the resulting gap increases.

Table 6. Calculated gap distances.

Load (*P*) (kN)	Length (*L*) (cm)	Thickness (cm)	Deflection (*y*) (cm)	θ (degrees)	Gap (cm)
0.89	2.95	0.95	–0.25	2.09	0.92
2.22	2.95	1.27	–0.26	2.20	1.24
2.22	2.95	1.59	–0.13	1.13	1.58

The second method of gap opening scaling with the panel thickness would be driven by the internal pressure (*P*) as the pin is plunged into the panel as illustrated in figure 32.

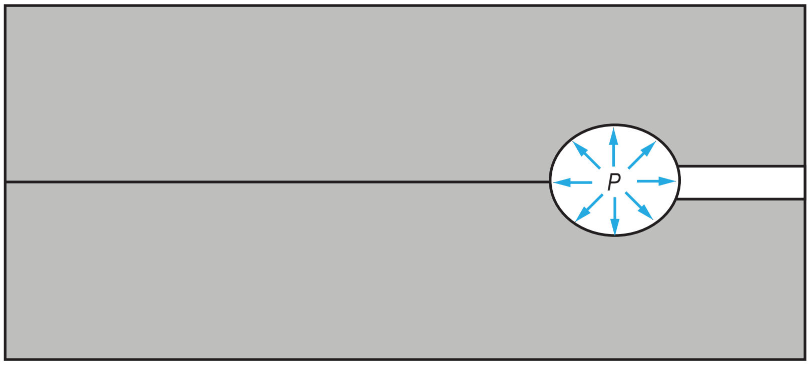

Figure 32. Internal pressure (*P*) around the tool opening the weld seam gap.

Aluminum and its alloys form a protective oxide coating. This oxide formation is almost instantaneous and follows a parabolic rate until an equilibrium thickness of 1–2 nm is formed. Although temperature, moisture, and alloying composition can affect the rate of oxidization, it is in all cases self-limiting unless fractured. This oxide is not readily removed and requires fracturing either through the application of loads or mechanical abrasives.

It is expected that aluminum alloys with increased lithium content such as AA2195 and 2099 would form a thicker oxide than those with less, such as AA2219. The same would hold for alloys with increased Mg content such as AA7075.

The studies in the literature on the lazy Z have concluded that nonoptimized parameters have been responsible for the reduction observed in mechanical properties. This is similar to studies at the NASA MSFC in which the lazy Z feature observed in SRFSWs was mitigated by modifying the weld parameters to include a tool offset.

As the oxidation rate is noted to increase with increasing temperature, it is conceivable that the faying surface would be prone to increased oxidation during the FSW if exposed to air. At the estimated FSW temperature of Al alloys (530–580 °C), the oxidation behavior rate is noted to change from parabolic to linear.

It is generally assumed that minimal entrained air enters the faying surface during a butt weld. However as the weld panels increase in thickness, it has been observed that gaps open in advance of the weld tool. It is theorized that this increasing gap, especially for SRFSWs, may provide a passageway for air to enter, causing enhanced oxidation at the elevated temperatures. This would be further exacerbated if eutectic phases formed along grain boundaries and locally melted at the welding temperature. Exposure to air at these temperatures would oxidize these molten regions along the grain boundaries. Studies have proposed that localized melting can occur in FSWs, especially at higher tool rotations.[34–35] However, evidence of melting is noted to become obscure in the microstructure that has undergone high levels of strain.[34]

TEM/STEM images show a eutectic microstructure in Cu-rich grains at the grain boundary. Since the eutectic has a melting temperature of 548 °C, it is possible that the FSWs experience these temperatures, especially at higher tool rotations.[33] Should these temperatures be reached, the eutectic could liquate, forming a liquid at the grain boundaries. This may correspond to the observation of thickened grain boundaries within the linear features observed in the FSWs investigated. Once liquated, these regions would be prone to enhanced oxidation resulting in brittle grain boundary phases.

If oxygen is entrained with air introduced within the gap opening, its rate would also be expected to be affected by diffusion within this region. The rate of oxidation would compete between the oxygen diffusion to the metal versus the depletion of oxygen from the gap. Thus, this occurrence could also depend on time at temperature as affected by the process parameters of tool rotation and travel velocity.

The chemical composition will also affect the resulting second phases present in the panels. Cu content can vary especially in AA2219. Higher Cu concentrations would yield more excess θ phase, which could explain variation over the years with different lots of AA2219. Similar concerns would be expected with variations in both Cu and Li content in the AA2195/AA2099 series of alloys. On the basis of the principal observations and a data review concerning oxidation reformation on 0.95 cm (0.375 in)-, 1.27 cm (0.5 in)-, and 1.59 cm (0.625 in)-thick AA2219-T87/AA2219-T87 Al weld quality and properties, it was concluded that delayed weld times from preweld cleaning up to 188 hr do not adversely affect the weld quality or properties.

6. SUMMARY

As thicker oxides require temperatures in excess of 500 °C to form, this study proposed that the formation of oxides occurs during the SRFSW process. The aspects of formation considered are:

(1) The geometry of the gap closure.

(2) Driving force to open the gap—either by internal pressure or cantilever beam bending.

(3) Obstacles to oxidation (factors affecting oxidation rate).

Delays in cleaning time are not expected to affect the weld quality of the solid-state SRFSW joining process. The seemingly random occurrence of ROD suggests there is an underlying cause. Understanding this cause and effect would improve the robustness of the SRFSW process. Possible causes include:

(1) Variations in amount of Cu or Li in the workpiece.

(2) Formation of eutectic structure in high Cu content alloys.

(3) Higher temperature (i.e. higher RPM) in the SRFSW configuration may promote oxidation. SRFSWs are considered to be hotter welds due to the lack of the backing anvil heat sink.

(4) Gap separation of thicker panels in advance of the FSW tool may provide a pathway for entrained air during the FSW process. This may be due to internal pressure, elastic deformation, or insufficient clamping.

Incorporation of a purge gas during the SRFSW process may be needed to mitigate oxide formation, especially in thicker workpieces. Further documentation of air entrainment should evaluate whether the occurrence of oxidation is predominately on the crown or root side.

While the lazy S feature was not observed in the metallographs of the SRFSWs in which oxides were found, it may be worthwhile to image unetched specimens of 1.59 cm (0.625 in) panel thickness in an SEM.

REFERENCES

1. Krishnan, K.N.: “On the formation of onion rings in friction stir welds,” *Mat. Sci. Eng. A*, Vol. 327, No. 3, pp. 246–251, 2002.

2. Larsson, H.; Karlsson, L.; Stoltz, S.; and Bergqvist, E.L.: “Joining of dissimilar Al alloys by friction stir welding,” 2nd Intl. Symp. on Friction Stir Welding, Gothenburg, Sweden, June 27–29, 2000.

3. Carter, R.W.: “Auto-adjustable tool for self-reacting and friction stir welding,” US patent #6758382B1, July 6, 2004.

4. Li, B.; Shen, Y.; and Hu,W.: “The study on defects in aluminum 2219-T6 thick butt friction stir welds with the application of multiple non-destructive testing methods,” *Materials and Design*, Vol. 32, No. 4, pp. 2073–2084, 2011.

5. Nunes, Jr., A.C.; Pendleton, M.L.; Brooke, S.A.; Russell, C.K.:“Effects of Fusion Tack Welds on Self-Reacting Friction Stir Welds,” NASA/TM—2012–217474, November 2012.

6. Chen, H.-B.; Yan, K.; Lin, T.; Chen, S-B.; Jiang, C-Y.; Zhao, Y.: “The investigation of typical welding defects for 5456 aluminum alloy friction stir welds,” *Mat. Sci. Eng. A*, Vol. 433, No. 1-2, pp. 64–69, 2006.

7. Klages, H. K.: “The ‘Lazy S’ feature in friction stir welding of AA2099 Aluminum-Lithium alloy,” MS Thesis, Navy Postgraduate School, Monterey, CA, 64 pp., December 2007.

8. Leonard, A.J.; and Lockyer, S.A.: “Flaws in friction stir welds,” 4th Intl. Symp. on Friction Stir Welding, Park City, Utah, May 14–16, 2003.

9. Liu, H.J.; Chen, Y.C.; Feng, J.C.: “Effect of zigzag line on the mechanical properties of friction stir welded joints of an Al–Cu alloy,” *Scripta Materialia*, Vol. 55, No. 3, pp. 231–234, 2006.

10. Nunes, Jr. A. C.: “Metal Flow in Friction Stir Welding,” in *Proc. MS&T Conference*, October 15–19, 2006, ASM International, Cincinnati, OH.

11. Field, D.P.; Nelson, T.W; Hovanski, Y.; and Jata, K.V.: “Heterogeneity of Crystallographic Texture in Friction Stir Welds of Aluminum,” *Metall. Mater. Trans. A*, Vol. 32, No. 11, pp. 2869–2877, 2001.

12. Sato, Y.S. Kokawa, H. Ikeda, K.; et al.: “Microtexture in the friction-stir weld of an aluminum alloy,” *Metall. Mater. Trans. A*, Vol. 32, No. 4, pp. 941–948, 2001.

13. Park, S.H.C.; Sato, Y.S.; and Kokawa, H.: "Microstructural factors governing hardness in friction-stir welds of solid-solution-hardened Al alloys," *Metall. Mater. Trans. A*, Vol. 32, No. 12, pp. 3033–3042, 2001.

14. Sato, Y.S.; Yamashita, F.; Sugiura, Y.; et al.: "FIB-assisted TEM study of an oxide array in the root of a friction stir welded aluminum alloy," *Scripta Materialia*, Vol. 50, No. 3, pp. 365–369, 2004.

15. Crawford, R.; Cook, G.E.; Strauss, A.M.; et al: "Experimental defect analysis and force prediction simulation of high weld pitch friction stir welding," *Sci. Technol. Weld. Joi.*, Vol. 11, No. 6, pp. 657–665, 2006.

16. Liu, H.J.; Fujii, H,; Maeda, M.; and Nogi, K.: "Tensile fracture location characterizations of friction stir welded joints of different aluminum alloys," *J. Mater. Sci. Technol.*, Vol. 20, No. 1, pp. 103–105, 2004.

17. Long, X.; and Khanna, S.K.: "Modelling of electrically enhanced friction stir welding process using finite element method," *Sci. Technol. Weld Joi.*, Vol. 10, No. 4, pp. 482–487, 2005.

18. Kim, Y.G. Fujii, H, Tsumura, T.; et al.: "Three defect types in friction stir welding of aluminum die casting alloy," *Mater. Sci. Eng. A-Struct.*, Vol. 415, No. 1-2, pp. 250–254, 2006.

19. Hart, R.K.: "The oxidation of aluminum in dry and humid oxygen atmospheres," *Proceed. Royal Society of London, Series A. Mathematics & Physical Sciences*, Vol. 236, No. 1204, pp. 68–88, doi: 10.1098/rspa.1956.0113, 1956.

20. Jeurgens, L.P.H.; Sloof, W.G.; Tichelaar, F.D.; and Mittemeijer, E.J.: "Structure and morphology of aluminum-oxide films formed by thermal oxidation of aluminum," *Thin Solid Films*, Vol. 418, No. 2, pp. 89–101, 2002.

21. Doherty, P.E.; and Davis, R.S.: "Direct Observation of the Oxidation of Aluminum Single-Crystal Surfaces," *J. Appl. Phys.*, Vol. 34, No. 3, pp. 619–628, 1963.

22. Thomas, K.; and Roberts, M.W.: "Direct observation in the electron microscope of oxide layers on aluminum," *J. Appl. Phys.*, Vol. 32, No. 1, pp. 70–75, 1961.

23. Steinheil, A.: "Structure and growth of thin surface films on metal through oxidation in air," *Ann. Phys.*, Vol. 19, No. 5, pp. 465–483, 1934, NASA-TT-F-11905, English translation, 1968.

24. Trunov, M.A.; Schoenitz, M.; Zhu, X.; and Dreizin, E.L.: "Effect of polymorphic phase transformations in Al_2O_3 film on oxidation kinetics of aluminum powders," *Combustion & Flame*, Vol. 140, pp. 310–318, 2005.

25. Sanchez-Lopez, J.C.; Gonzalez-Elipe, A.R.; and Fernandez, A.: "Passivation of nanocrystalline Al prepared by the gas phase condensation method: An X-ray photoelectron spectroscopy study," *J. Mater. Res.*, Vol. 13, No. 3, pp. 703–710, 1998.

26. Smeltzer, W.W.: "Oxidation of Aluminum in the Temperature Range of 400º to 600º C," *J. Electrochem. Soc.*, Vol. 103, No. 4, pp. 209–214, 1956.

27. Jeurgens, L.P.H.; Sloof, W.G.; Tichelaar, F.D.; and Mittemeijer, E.J.: "Growth kinetics and mechanisms of aluminum-oxide films formed by thermal oxidation of aluminum," *J. Appl. Phys.*, Vol. 92, pp. 1649–1656, 2002.

28. Bergsmark, E.; Simensen, C.J.; and Kofstad, P.: "The oxidation of molten aluminum," *Mater. Sci. Eng. A-Struct.*, Vol. 120, pp. 91–95, 1989.

29. Thiele, W.: "The Oxidation of Melts of Aluminum and Aluminum Alloys," Aluminum, Vol. 38, pp. 707–786, 1962.

30. Cochran, C.N.; Belitskus, D.L.; and Kinosz, D.L.: "Oxidation of aluminum-magnesium melts in air, oxygen, flue gas, and carbon dioxide," *Metall. Trans. B*, Vol. 8, No. 1, pp. 323–332, 1977.

31. Oh, Y-J.; Mun J-I. Kim,; and J-H.: "Effects of alloying elements on microstructure and protective properties of Al2O3 coatings formed on aluminum alloy substrates by plasma electrolysis," *Surface and Coatings Technology*, Vol. 204, No 1–2, pp. 141–148, 2009.

32. Record, J.H.; Covington, J.L.; Nelson, T.W.; et al.: "A Look at the Statistical Identification of Critical Process Parameters in Friction Stir Welding," *Welding Journal*, Vol. 86, No. 4, pp. 97-s–103-s, 2007.

33. Schneider, J.A.; Stromberg, R.; Schilling, P.; et al: "Processing Effects on the Friction Stir Weld Stir Zone," *Welding Journal*, Vol 92, No. 1, pp. 11-s–19-s, 2013.

34. Threadgill, P.L.; Leonard, A.J.; Shercliff, H.R.; and Withers, P.J.: "Friction stir welding of aluminum alloys," *Int. Mater. Rev.*, Vol. 54, No. 2, pp. 49–93, 2009.

35. Alfaro-Mercado, U.; and Biallas, G.: "Incipient Melting and Corrosion Properties of Friction Stir Welded AA2024-T3 Joints," in *Proc. 12th Intl. Conf. Al. Alloys*, September 5–9, 2010, Yokohama Japan, The Japan Institute of Light Metals, pp. 978–983.

REPORT DOCUMENTATION PAGE

Form Approved
OMB No. 0704-0188

1. REPORT DATE *(DD-MM-YYYY)* 01–08–2018	**2. REPORT TYPE** Technical Memorandum	**3. DATES COVERED** *(From - To)*

4. TITLE AND SUBTITLE
Mechanisms of Oxide Formation in the Self-Reacting Friction Stir Weld Process

5a. CONTRACT NUMBER

5b. GRANT NUMBER

5c. PROGRAM ELEMENT NUMBER

6. AUTHOR(S)
J.A. Schneider,* J.P. Norris,** P. Chen,** and A.C. Nunes, Jr.

5d. PROJECT NUMBER

5e. TASK NUMBER

5f. WORK UNIT NUMBER

7. PERFORMING ORGANIZATION NAME(S) AND ADDRESS(ES)
George C. Marshall Space Flight Center
Huntsville, AL 35812

8. PERFORMING ORGANIZATION REPORT NUMBER
M–1467

9. SPONSORING/MONITORING AGENCY NAME(S) AND ADDRESS(ES)
National Aeronautics and Space Administration
Washington, DC 20546–0001

10. SPONSORING/MONITOR'S ACRONYM(S)
NASA

11. SPONSORING/MONITORING REPORT NUMBER
NASA/TM—2018–219863

12. DISTRIBUTION/AVAILABILITY STATEMENT
Unclassified-Unlimited
Subject Category 38
Availability: NASA STI Information Desk (757–864–9658)

13. SUPPLEMENTARY NOTES
Prepared by the Materials & Processes Laboratory, Engineering Directorate
*The University of Alabama in Huntsville, Huntsville, AL, **Jacobs ESSST, Marshall Space Flight Center

14. ABSTRACT

This study evaluates the effect of potential contamination due to a 188-hr delay between preweld cleaning and weld completion on a self-reacting friction stir weld. Tensile testing and metallographic imaging reveal the contamination's effect on the quality of various thickness panels of AA2219-T87. Tensile specimens were tested at room temperature and at cryogenic conditions of liquid nitrogen and liquid hydrogen. No detrimental effect on weld quality, as determined by weld strength, was reported for cleaning delays of 48, 120, 168, 240 or 288 hr. While no trends were established in this study, outliers appeared in terms of ultimate tensile strength, and met the minimum acceptance criteria. This report examines those outliers and their possible causes.

15. SUBJECT TERMS
Friction stir welding, entrapped oxidation in FSW, mechanical properties of FSW

16. SECURITY CLASSIFICATION OF:			**17. LIMITATION OF ABSTRACT**	**18. NUMBER OF PAGES**	**19a. NAME OF RESPONSIBLE PERSON**
a. REPORT	**b. ABSTRACT**	**c. THIS PAGE**			STI Help Desk at email: help@sti.nasa.gov
U	U	U	UU	52	**19b. TELEPHONE NUMBER** *(Include area code)* STI Help Desk at: 757–864–9658

National Aeronautics and
Space Administration
IS02
George C. Marshall Space Flight Center
Huntsville, Alabama 35812